Eur. Phys. J. C manuscript No.
(will be inserted by the editor)

Towards an Understanding of the Correlations in Jet Substructure

Report of BOOST2013, hosted by the University of Arizona, 12^{th}-16^{th} of August 2013.

D. Adams[1], A. Arce[2], L. Asquith[3], M. Backovic[4], T. Barillari[5], P. Berta[6], D. Bertolini[2], A. Buckley[8], J. Butterworth[9], R. C. Camacho Toro[10], J. Caudron[9], Y.-T. Chien[11], J. Cogan[12], B. Cooper[9], D. Curtin[17], C. Debenedetti[18], J. Dolen[9], M. Eklund[22], S. El Hedri[22], S. D. Ellis[22], T. Embry[22], D. Ferencek[23], J. Ferrando[24], S. Fleischmann[16], M. Freytsis[25], M. Giulini[21], Z. Han[27], D. Hare[4], P. Harris[4], A. Hinzmann[4], R. Hoing[4], A. Hornig[22], M. Jankowiak[4], K. Johns[28], G. Kasieczka[23], T. Knight[24], G. Kasieczka[29], R. Kogler[30], W. Lampl[4], A. J. Larkoski[4], C. Lee[31], R. Leone[31], P. Loch[31], D. Lopez Mateos[27], H. K. Lou[27], M. Low[27], P. Maksimovic[32], I. Marchesini[32], S. Marzani[32], L. Masetti[33], R. McCarthy[32], S. Menke[32], D. W. Miller[35], K. Mishra[36], B. Nachman[32], P. Nef[4], F. T. O'Grady[24], A. Ovcharova[23], A. Picazio[37], C. Pollard[38], B. Potter Landua[29], C. Potter[29], S. Rappoccio[39], J. Rutherfoord[40], G. P. Salam[10,11], J. Schabinger[23], A. Schwartzman[4], M. D. Schwartz[27], B. Shuve[43], P. Sinervo[44], D. Soper[45], D. E. Sosa Corral[45], M. Spannowsky[32], E. Strauss[34], M. Swiatlowski[4], J. Thaler[34], C. Thomas[34], E. Thompson[1], N. V. Tran[36], J. Tseng[36], E. Usai[36], L. Valery[36], J. Veatch[23], M. Vos[23], W. Waalewijn[4], and C. Young[47]

[1] *Columbia University, Nevis Laboratory, Irvington, NY 10533, USA*
[2] *Duke University, Durham, NC 27708, USA*
[3] *Argonne National Laboratory, Lemont, IL 60439, USA*
[4] *SLAC National Accelerator Laboratory, Menlo Park, CA 94025, USA*
[5] *Deutsches Elektronen-Synchrotron, DESY, D-15738 Zeuthen, Germany*
[6] *Cornell University, Ithaca, NY 14853, USA*
[7] *Lund University, Lund, SE 22100, Sweden*
[8] *University of Edinburgh, EH9 3JZ, UK*
[9] *University College London, WC1E 6BT, UK*
[10] *LPTHE, UPMC Univ. Paris 6 and CNRS UMR 7589, Paris, France*
[11] *CERN, CH-1211 Geneva 23, Switzerland*
[12] *CAFPE and U. of Granada, Granada, E-18071, Spain*
[13] *McGill University, Montreal, Quebec H3A 2T8, Canada*
[14] *Iowa State University, Ames, Iowa 50011, USA*
[15] *Rutgers University, Piscataway, NJ 08854, USA*
[16] *Bergische Universitaet Wuppertal, Wuppertal, D-42097, Germany*
[17] *YITP, Stony Brook University, Stony Brook, NY 11794-3840, USA*
[18] *University of Manchester, Manchester, M13 9PL, UK*
[19] *UNESP - Universidade Estadual Paulista, Sao Paulo, 01140-070, Brazil*
[20] *INFN and University of Naples, IT80216, Italy*
[21] *University of Geneva, CH-1211 Geneva 4, Switzerland*
[22] *University of Washington, Seattle, WA 98195, USA*
[23] *Instituto de Física Corpuscular, IFIC/CSIC-UVEG, E-46071 Valencia, Spain*
[24] *University of Glasgow, Glasgow, G12 8QQ, UK*
[25] *Berkeley National Laboratory, University of California, Berkeley, CA 94720, USA*
[26] *Universidad de Buenos Aires, AR-1428, Argentina*
[27] *Harvard University, Cambridge, MA 02138, USA*
[28] *Weizmann Institute, 76100 Rehovot, Israel*
[29] *Universitaet Hamburg, DE-22761, Germany*
[30] *Universitaet Heidelberg, DE-69117, Germany*
[31] *University of Arizona, Tucson, AZ 85719, USA*
[32] *IPPP, University of Durham, Durham, DH1 3LE, UK*
[33] *Universitaet Mainz, DE 55099, Germany*
[34] *MIT, Cambridge, MA 02139, USA*
[35] *University of Chicago, IL 60637, USA*
[36] *Fermi National Accelerator Laboratory, Batavia, IL 60510, USA*
[37] *Indiana University, Bloomington, IN 47405, USA*
[38] *University of California, Davis, CA 95616, USA*
[39] *Johns Hopkins University, Baltimore, MD 21218, USA*
[40] *INFN and University of Pisa, Pisa, IT-56127, Italy*
[41] *Texas A & M University, College Station, TX 77843, USA*
[42] *INFN and University of Calabria, Rende, IT-87036, Italy*
[43] *Brown University, Richmond, RI 02912, USA*
[44] *Yale University, New Haven, CT 06511, USA*
[45] *CEA Saclay, Gif-sur-Yvette, FR-91191, France*
[46] *University of Illinois, Chicago, IL 60607, USA*
[47] *University of California, Berkeley, CA 94720, USA*

Abstract Abstract for BOOST2013 report

Keywords boosted objects · jet substructure · beyond-the-Standard-Model physics searches · Large Hadron Collider

1 Introduction

Jet substructure has been around a while now, and it's time to study the correlations between the plethora of observables that have been developed and used. Previous BOOST reports [?,?,?] studied some of these things.

2 Monte Carlo Samples

2.1 Quark/gluon and W tagging

Samples were generated at $\sqrt{s} = 8$ TeV for QCD dijets and W^+W^- pairs decaying hadronically off a (pseudo) scalar resonance. The QCD events were split into subsamples of gg and $q\bar{q}$ events, allowing for tests of both W and quark-gluon discrimination.

Individual quark and gluon samples were produced at leading order (LO) using MadGraph5, while W^+W^- samples were generated using the JHU Generator to allow for separation of longitudinal and transverse polarizations. Both were produced in exclusive p_T bins of 100 GeV and generated using CTEQ6L1 PDFs. The slicing parameter was chosen to be the p_T of any final state parton or W. At the parton-level the p_T bins investigated were 300-400 GeV, 500-600 GeV and 1.0-1.1 TeV. Since no matching was performed, a cut on any parton was equivalent. These were then showered through Pythia8 (version 8.176) using the default tune 4C.

The showered events were clustered with FastJet 3.03 using the anti-k_t algorithm with jet radii of $R = 0.4, 0.8, 1.2$. In both signal and background an upper and lower cut on the leading jet p_T is applied after showering/clustering, to ensure similar p_T spectra for signal and background in each bin. The bins in leading jet p_T that are investigated in the W-tagging and q/g tagging studies are 300-450 GeV, 500-650 GeV, 1.0-1.2 TeV.

2.2 Top tagging

Samples were generated at $\sqrt{s} = 14$ TeV. Standard Model dijet and top pair samples were produced with Sherpa 2.0.0, with matrix elements with up to two extra partons matched to the shower. The top samples included only hadronic decays and were generated in exclusive p_T bins of width 100 GeV, taking as slicing parameter the maximum of the top/anti-top p_T. The QCD samples were generated with a cut on the leading parton-level jet p_T, where parton-level jets are clustered with the anti-k_t algorithm with jet radius $R = 1.2$. The matching scale is selected to be $Q_{\rm cut} = 40, 60, 80$ GeV for the $p_{T\,\rm min} = 600, 1000$, and 1500 GeV bins, respectively.

The analysis again relies on FastJet 3.0.3 for jet clustering and calculation of jet substructure observables, with the same cuts applied after showering and clustering as for $\sqrt{s} = 8$ TeV data.

3 Jet Algorithms and Grooming Approaches

Describe the jet algorithms and grooming approaches that we will use in the report. Give the nomenclature that we will use to refer to e.g. the groomed mass in the rest of the report.

4 Substructure Variables/Taggers

In this section, we describe the observables that we consider in this study. Originally we considered a larger set of observables but in the final analysis we reduced redundant observables in the final set for presentation purposes.
The list of observables for quark vs. gluon discrimination is as follows:

- mass: this is the plain jet mass
- 1-subjettiness, τ_1^β: the N-subjettiness uses one-pass k_T axis optimization where we consider $\beta = 1, 2$
- 1-point energy correlation functions, C_1^β: the energy correlation functions consider $\beta = 0, 1, 2$
- Qjet volatility, $\Gamma_{\rm Qjet}$: the number of trees considered is $N_{\rm trees} = 25$, the rigidity factor is $\alpha = 0.1$, the truncation factor is 0.01, and the pruning parameters are $D_{\rm cut} = 0.5$ and $z_{\rm cut} = 0.1$
- number of constituents ($N_{\rm constits}$)

The list of observables for W vs. gluon discrimination is as follows:

- mass: same as in the q vs. g case
- trimmed mass, $m_{\rm trimmed}$: the parameter values are $f_{\rm cut} = 0.03$ and $r_{\rm filt} = 0.2$
- pruned mass, $m_{\rm pruned}$: the parameter values are $D_{\rm cut} = 0.5$ and $z_{\rm cut} = 0.1$

- soft drop mass, $m^{\beta}_{\text{softdrop}}$: z_{cut} is set always to 0.1, we consider $\beta = 0, 2$ where $\beta = 0$ is a generalization of the modified mass drop tagger
- 2-point energy correlation functions, $C_2^{\beta=1}$: we also considered $\beta = 2$ but it showed poor discrimination power
- N-subjettiness ratio, $\tau_2/\tau_1(\beta = 2)$: the N-subjettiness uses one-pass k_T axis optimization, we also considered $\beta = 2$ but it showed poor discrimination power
- Qjet volatility: same as in the q vs. g case

We now describe the list of observables/taggers considered for top tagging. Note that for trimming, the subjet identification is optimized for identifying soft radiation, *not* for reconstructing the hard decay products of the top. Pruning does not even contain an inherent subject identification step. For both trimming and pruning, we introduce an arbitrary method for reconstructing the subjets corresponding to the b and W decay products for a fair comparison with other top taggers, but the W reconstruction is consequently poorer than for algorithms that are optimized for W identification inside the top.

Johns Hopkins Tagger: Re-cluster the jet using the Cambridge-Aachen algorithm. The jet is iteratively declustered, and at each step the softer prong is discarded if its p_{T} is less than $\delta_p\, p_{\text{T jet}}$. This continues until both prongs are harder than the p_{T} threshold, both prongs are softer than the p_{T} threshold, or if they are too close ($|\Delta\eta_{ij}|+|\Delta\phi_{ij}| < \delta_R$); the jet is rejected if either of the latter conditions apply. If both are harder than the p_{T} threshold, the same procedure is applied to each: this results in 2, 3, or 4 subjets. If there exist 3 or 4 subjets, then the jet is accepted: the top candidate is the sum of the subjets, and W candidate is the pair of subjets closest to the W mass. The output of the tagger is m_t, m_W, and θ_{h}, a helicity angle defined as the angle, measured in the rest frame of the W candidate, between the top direction and one of the W decay products.

HEPTopTagger: Re-cluster the jet using the Cambridge-Aachen algorithm. The jet is iteratively de-clustered, and at each step the softer prong is discarded if $m_1/m_{12} > \mu$ (there is not a significant mass drop). Otherwise, both prongs are kept. This continues until a prong has a mass $m_i < m$, at which point it is added to the list of subjets. Filter the jet using $R_{\text{filt}} = \min(0.3, \Delta R_{ij})$ (where ΔR_{ij} is the distance between the two hardest subjets). Select the three subjets whose invariant mass is closest to m_t. The output of the tagger is m_t, m_W, and θ_{h}, a helicity angle defined as the angle, measured in the rest frame of the W candidate, between the top direction and one of the W decay products.

Trimming: Re-cluster the jet using the k_{T} algorithm and radius R_{trim}. Discard all subjets with $p_{\text{T sj}}/p_{\text{T jet}} < f_{\text{cut}}$. A W candidate is reconstructed as follows: if there are two subjets, the highest-mass subjet is the W candidate; if there are three subjets, the two subjets with the smallest invariant mass comprise the W candidate. In the case of only one subjet, no W is reconstructed.

Pruning: Re-cluster the jet using the Cambridge-Aachen algorithm. At each step, discard the softer branch if $\min(p_{\text{T1}}, p_{\text{T2}})/p_{\text{T12}} < z_{\text{cut}}$ and $\Delta R_{12} > 2R_{\text{cut}} m_{\text{jet}}/p_{T,\,\text{jet}}$. Subjets are found by de-clustering the pruned jet by up to three splittings. A W candidate is reconstructed as follows: if there are two subjets, the highest-mass subjet is the W candidate; if there are three subjets, the two subjets with the smallest invariant mass comprise the W candidate. In the case of only one subjet, no W is reconstructed.

5 Quark-Gluon Discrimination

In this section we examine the differences between quark and gluon initiated jets in terms of the substructure variables, and to what extent these variables are correlated. Along the way, we attempt to provide some theoretical understanding of these observations. The motivation for these studies comes not only from the desire to "tag" a jet as being quark or gluon initiated, but also from the point of view of understanding the quark and gluon components to the QCD background to boosted boson and boosted top tagging.

5.1 Methodology

These studies use the qq and gg samples, described previously in Section 2.

Jets are reconstructed using the anti-k_{T} algorithm, and have various jet grooming approaches applied, as described in Section 3. The following event selection is then applied to these samples....(presumably this will vary depending on which kinematic bin is used, as will the actual samples used - maybe summarize in a table).

Go on to explain how we produce the ROC curves, how the BDT training is done etc.

Figure 1 shows a comparison of the quark and gluon samples in some basic kinematic distributions.

5.2 Single Variable Discrimination

Figure 2 the compares the quark and gluon samples in the mass distributions for the different groomers, and Figure 3 in the different substructure variables.

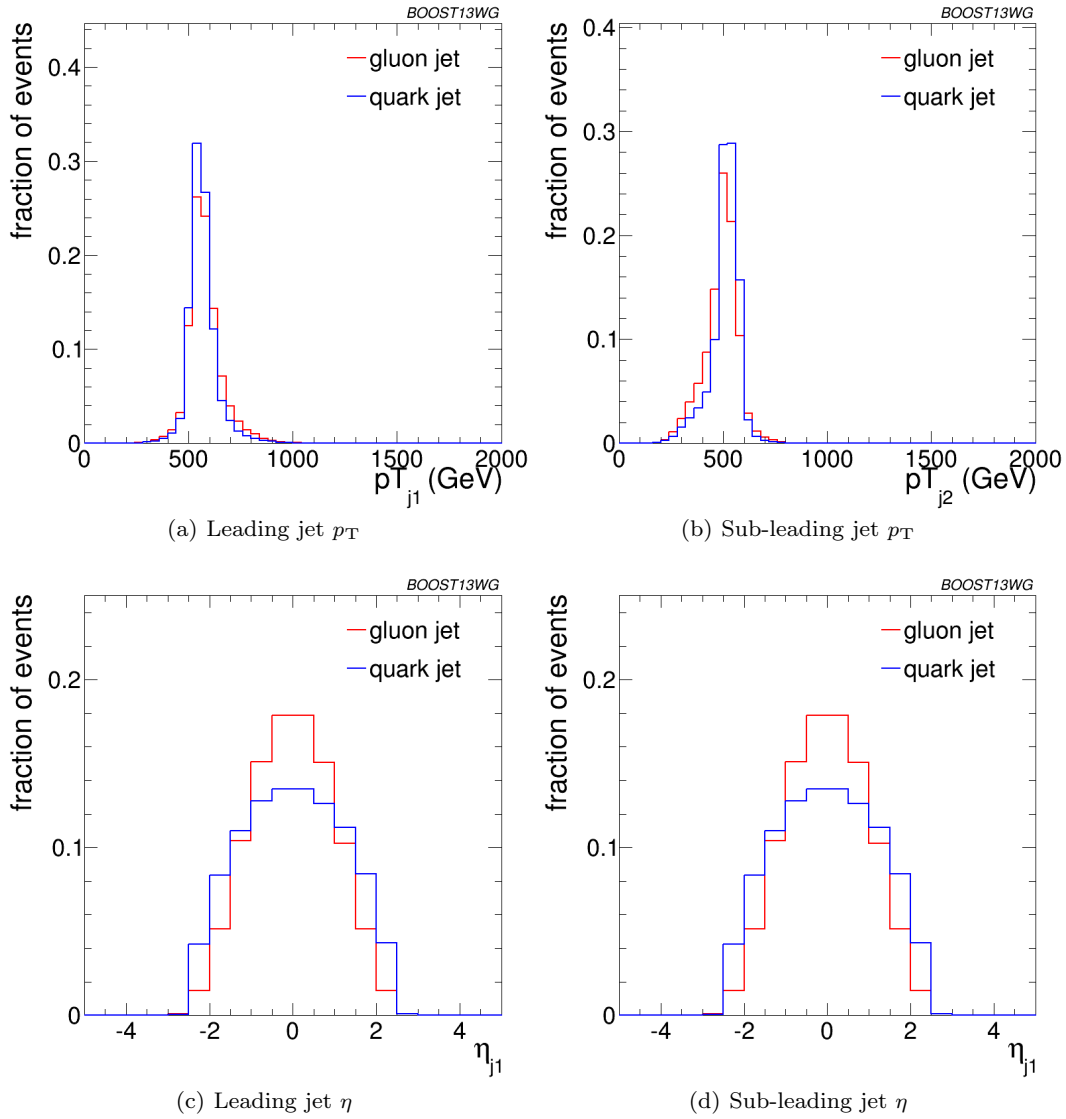

(a) Leading jet p_{T}

(b) Sub-leading jet p_{T}

(c) Leading jet η

(d) Sub-leading jet η

Fig. 1 Comparisons of quark and gluon distributions in the p_T 500 GeV bin using the anti-k_{T} R=0.8 algorithm: basic kinematic distributons.

Figure 4 shows the single variable ROC curves in the p_{T} 500 GeV bin for the anti-k_{T} R=0.8 algorithm, compared to the ROC curve for a BDT combination of all the variables. Only the ungroomed mass is shown. One can see that the single most discriminant variables are $\mathrm{n}_{\mathrm{constits}}$ and $C_1^{\beta=0}$.

We want to look also at:

- *Dependence on R.*
- *Dependence on pT.*

5.3 Correlations

Put in 2-D plots of correlations between variables (see theory discussions below)

5.4 Combined Performance of Quark-Gluon Tagging

Put in ROC curves of BDT combination of variables

5.5 QJets Volatility and p_TD ($C_1^{(\beta=0)}$)

Simple explanation of correlation, or why does combining volatility and p_TD improve quark versus gluon discrimination. p_TD ($C_1^{(\beta=0)}$) takes small (large) values for a jet with near-democratic energy sharing between particles and large (small) values when the energy of the jet is contained in a few particles. Because we expect gluons to radiate more particles, we expect that $p_TD_g < p_TD_q$ (or ${C_1^{(\beta=0)}}_g > {C_1^{(\beta=0)}}_q$). Now, we expect

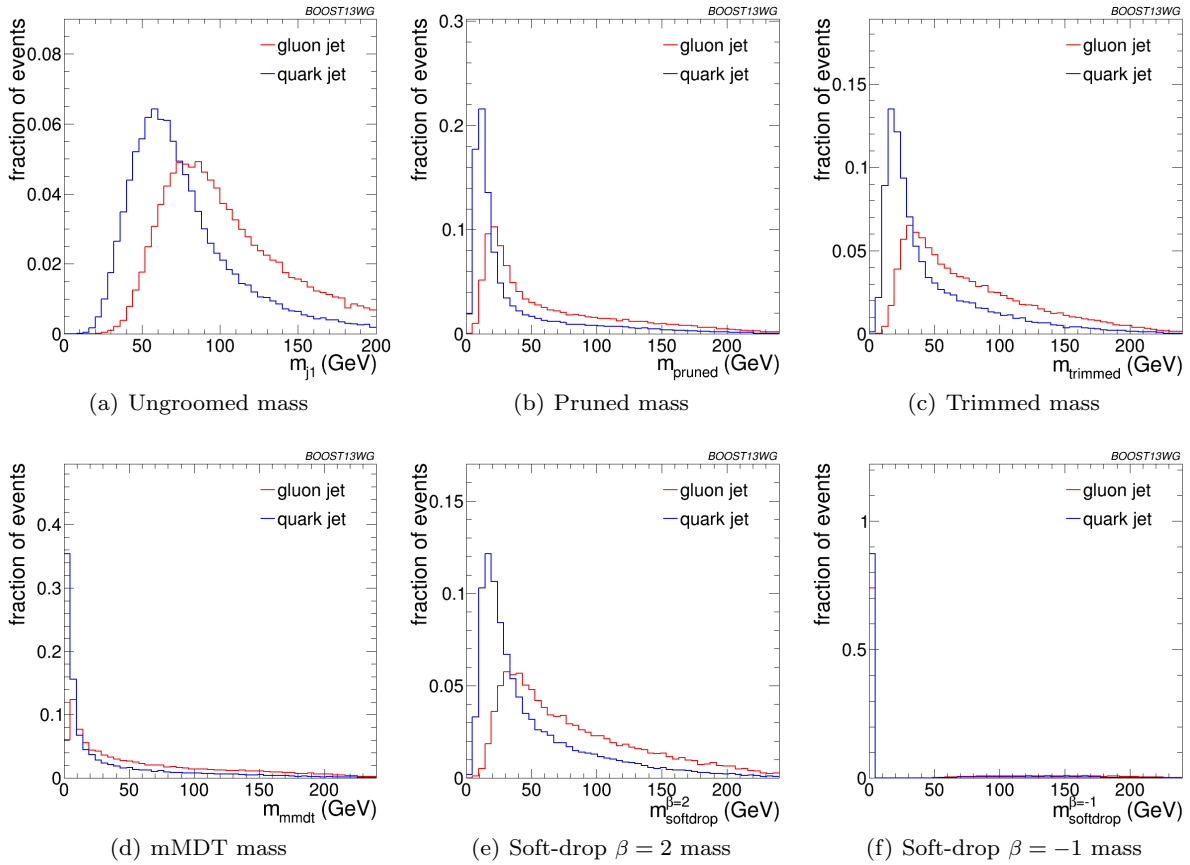

(a) Ungroomed mass (b) Pruned mass (c) Trimmed mass

(d) mMDT mass (e) Soft-drop $\beta = 2$ mass (f) Soft-drop $\beta = -1$ mass

Fig. 2 Comparisons of quark and gluon distributions in the p_T 500 GeV bin using the anti-k_T R=0.8 algorithm: leading jet mass distributions.

the volatility of gluon jets to be in general smaller than that of quark jets because there is a greater probability (by a factor of about $C_A/C_F = 9/4$) that there was a relatively hard emission in a jet that is not groomed away. By measuring both volatility and $p_T D$, we are sensitive to both regions of phase space: where a relatively hard emission dominates the mass of the jet as well as the region where many soft emissions set the jet mass.

The following is Steve's discussion of volatility difference between quarks and gluons:

Here is the (qualitative) thinking: typical QCD jet mass distributions look as illustrated on slide 17, although you should really be thinking in terms of plot versus m/p_T, since p_T is what sets the scale in the plot. Qualitatively there is a (very) large peak for $m/p_T \lesssim 0.1$ and you should think of these jets as having masses that arise from multiple soft emissions, some of which are at substantial angles. It is these components of the jet that are operated on by pruning (reducing the mass dramatically) and that yield the large volatility tail for QCD jets. For larger m/p_T values there is typically a shoulder (my description is clearest on a semi-log plot) that runs out to about $m/pT \sim 0.40.5$ (where the distribution decreases rapidly). These are the QCD jets (a small fraction of the total in a given p_T bin) that contain a hard, relatively large angle emission, which supplies the bulk of the jet mass. Such jets are effected only slightly by pruning and should exhibit much smaller volatility than the jets in the (smaller mass) peak region.

With that picture in mind and recalling that the size of the shoulder is given by low order perturbation theory (the probability of the one hard emission), we expect that the shoulder will be higher for gluons than for quarks (essentially by the usual C_A/C_F color charge factor), as suggested by the lower right plot on slide 17. Since the shoulder presumably plays a more important role for gluons (since it is larger), one would expect that the volatility distribution for gluons is narrower than quarks, as suggested in the upper left plot on slide 17. Am I making sense?

On the other hand, the volatility distribution plot indicates that the Q vs G distributions for your cuts are

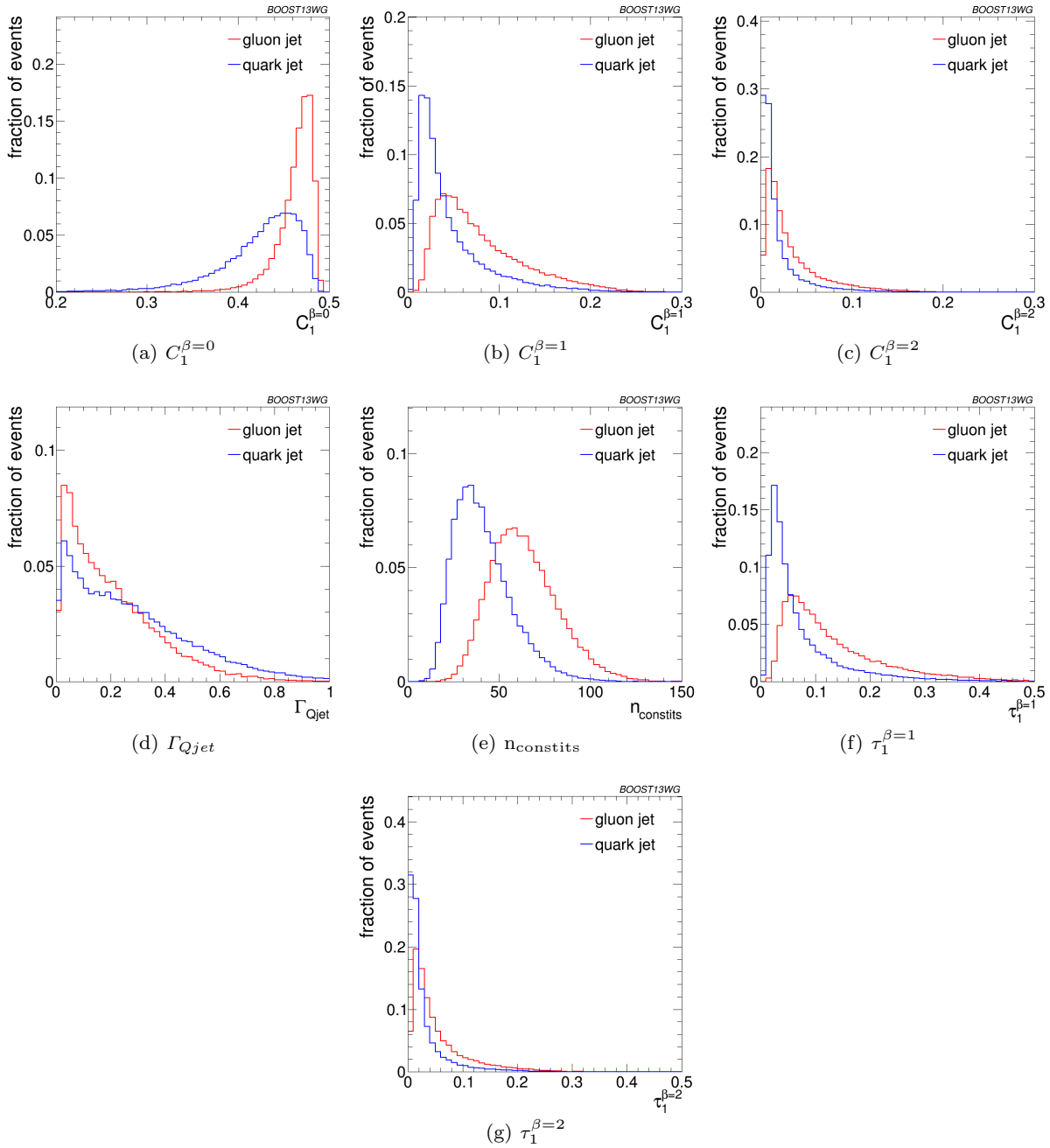

(a) $C_1^{\beta=0}$ (b) $C_1^{\beta=1}$ (c) $C_1^{\beta=2}$

(d) Γ_{Qjet} (e) $n_{constits}$ (f) $\tau_1^{\beta=1}$

(g) $\tau_1^{\beta=2}$

Fig. 3 Comparisons of the quark and gluon distributions in the p_T 500 GeV bin using the anti-k_T R=0.8 algorithm: substructure variables.

not really very different, which is presumably why it is not a very good discriminant by itself. But I expect this to depend it detail on where we are operating on the m/pT distributions. This leads to my request above. Your p_T bin is pretty broad and I dont expect the q and g samples to have the same shape within the bin. Of course, this may not be an issue, but I would like to check.

5.6 Comparison of Groomed Jet Masses

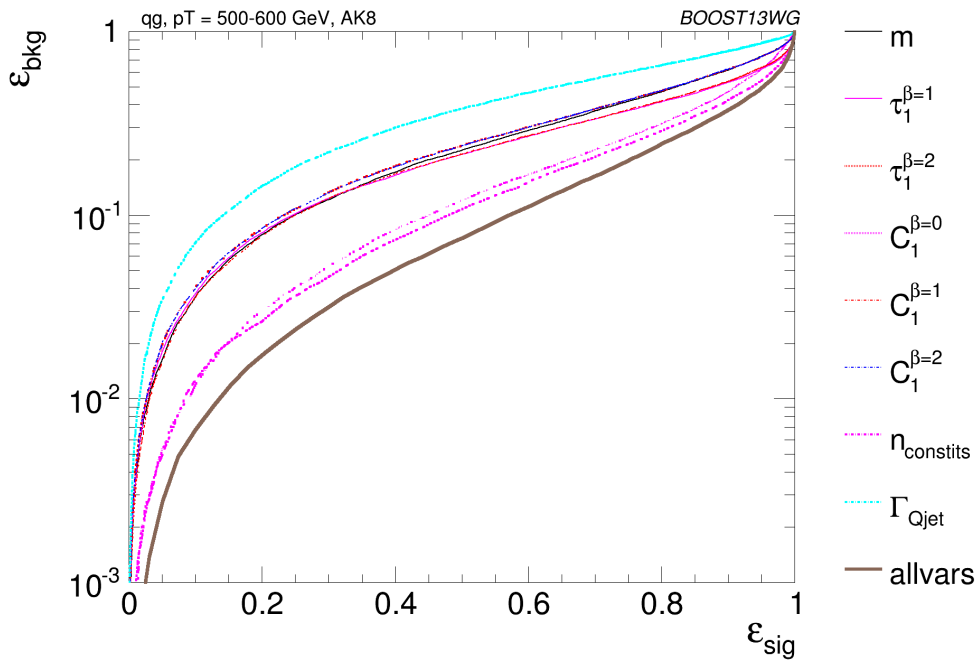

Fig. 4 The ROC curve for all single variables considered for quark-gluon discrimination in the p_T 500 GeV bin using the anti-k_T R=0.8 algorithm.

6 Boosted W-Tagging

In this section we study the performance of various groomed jet masses, substructure variables, and BDT combinations of groomed mass and substructure, in terms of the identification of a boosted hadronically decaying W signal aginst a gluon-gluon background. We produce Receiver Operating Characteristic (ROC) curves that elucidate the performance of the various groomed mass and substructure variables that are capable of providing discrimination between signal and background. A range of different distance parameter settings for the anti-k_T jet algorithm are explored, in a variety of kinematic regimes (lead jet p_T 300-450 GeV, 500-650 GeV, 1.0-1.2 TeV), to explore the performance as a function of jet radius and jet boost, and to see where substructure approaches may break down. The groomed mass and substructure variables are then combined in a Boosted Decision Tree (BDT), and the performance of the resulting BDT discriminant explored through ROC curves to understand the degree to which variables are correlated and exploiting the same information, and how this changes with jet boost and jet radius.

6.1 Methodology

These studies use the $X \rightarrow WW$ samples as signal and the gg samples to model the QCD background, described previously in Section 2. Whilst only gluonic backgrounds are explored here, the conclusions as to the dependence of the performance and correlations on the jet boost and radius have been verified to hold also for qq backgrounds. *To be checked!*

Jets are reconstructed using the anti-k_T algorithm, and have various jet grooming approaches applied, as described in Section 3. The following event selection is then applied to these samples....(presumably this will vary depending on which kinematic bin is used, as will the actual samples used - maybe summarize in a table).

Figure 5 shows a comparison of the leading jet p_T for the signal and background in the p_T 300-450 GeV bin, for the two different anti-k_T jet algorithm distance parameters explored in this bin (R=0.8 and R=1.2). Figures 6 and 7 show the same for the p_T 500-650 GeV bin and p_T 1.0-1.2 TeV bin respectively, where for the p_T 1.0-1.2 TeV bin the distance parameter R=0.4 is also explored.

Go on to explain how we produce the ROC curves, how the BDT training is done etc.

6.2 Single Variable Performance

In this section we will explore the performance of the various groomed jet mass and substructure variables in terms of discriminating signal and background, and how

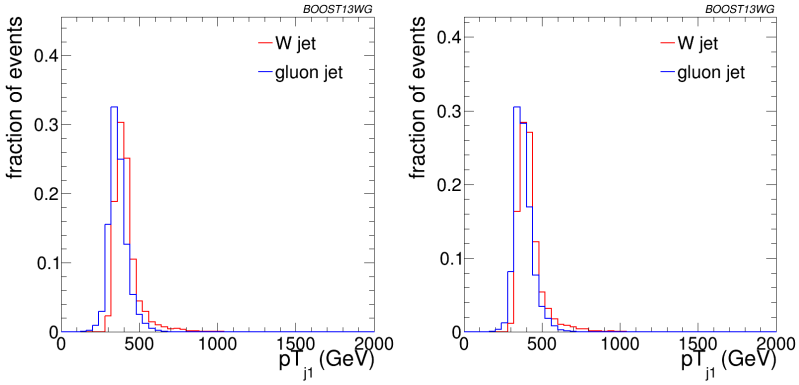

(a) anti-k_{T} R=0.8 (b) anti-k_{T} R=1.2

Fig. 5 Comparisons of the leading jet p_T spectrum of the gg background to the WW signal in the p_T 300-450 GeV bin using the different anti-k_{T} jet distance parameters explored.

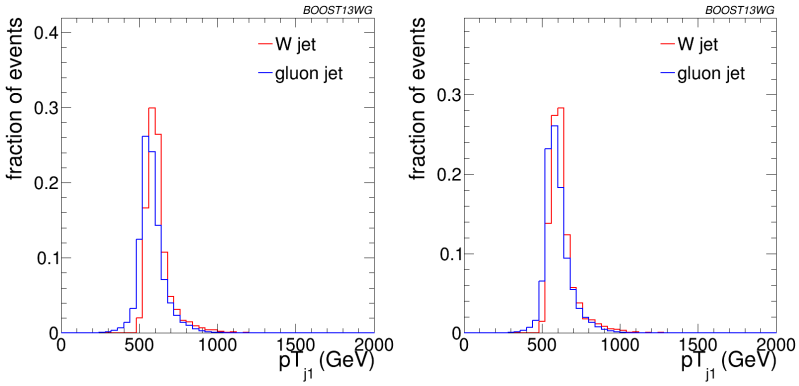

(a) anti-k_{T} R=0.8 (b) anti-k_{T} R=1.2

Fig. 6 Comparisons of the leading jet p_T spectrum of the gg background to the WW signal in the p_T 500-650 GeV bin using the different anti-k_{T} jet distance parameters explored.

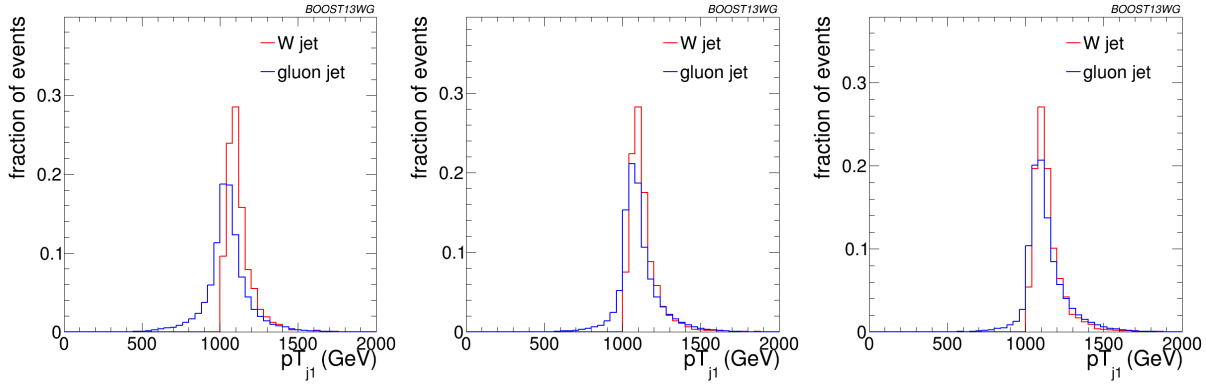

(a) anti-k_{T} R=0.4 (b) anti-k_{T} R=0.8 (c) anti-k_{T} R=1.2

Fig. 7 Comparisons of the leading jet p_T spectrum of the gg background to the WW signal in the p_T 1.0-1.2 TeV bin using the different anti-k_{T} jet distance parameters explored.

this performance changes depending on the kinematic bin and jet radius considered.

Figure 8 the compares the signal and background in terms of the different groomed masses explored for the anti-k_{T} R=0.8 algorithm in the p_T 500-650 bin. One can clearly see that in terms of separating signal and background the groomed masses will be significantly more performant than the ungroomed anti-k_{T} R=0.8 mass. Figure 9 compares signal and background in the different substructure variables explored for the same jet radius and kinematic bin.

Figures 10,11 and 12 show the single variable ROC curves compared to the ROC curve for a BDT combination of all the variables (labelled "allvars"), for each of the anti-k_{T} distance parameters considered in each of the kinematic bins. One can see that, in all cases, the "allvars" option is considerably more performant than any of the individual single variables considered, indicating that there is considerable complementarity between the variables, that will be explored further in the next section.

Although the ROC curves give all the relevant information, it is hard to compare performance quantitatively. In Figures 13, 14 and 15 are shown matrices which give the background rejection for a signal efficiency of 50% when two variables (that on the x-axis and that on the y-axis) are combined in a BDT. These are shown separately for each p_T bin and jet radius considered. The diagonal of these plots correspond to the background rejections for a single variable BDT, and can thus be examined to get a quantitative measure of the individual single variable performance, and to study how this changes with jet radius and momenta.

One can see that in general the most performant single variables are the groomed masses. However, in certain kinematic bins and for certain jet radii, $C_2^{\beta=1}$ has a background rejection that is comparable to or better than the groomed masses.

By comparing Figures 13(a), 14(a) and 15(b), we can see how the background rejection performance evolves as we increase momenta whilst keeping the jet radius fixed to R=0.8. Similarly, by comparing Figures 13(b), 14(b) and 15(c) we can see how performance evolves with p_T for R=1.2. The background rejection power of the groomed masses increases slowly with increasing p_T , with at most a factor two increase in rejection in going from the 300-450 GeV to 1.0-1.2 TeV bins. However, for a jet radius of R=0.8, the rejection power of $C_2^{\beta=1}$ increases dramatically with p_T , by a factor of 7 in going from the 300-450 GeV to 1.0-1.2 TeV bins. *Can we explain this?* Conversely, the background rejection of the other substructure variables (Γ_{Qjet} and $\tau_{21}^{\beta=1}$) slowly reduces with increasing p_T , at most decreasing by a factor of two.

By comparing the individual sub-figures of Figures 13, 14 and 15 we can see how the background rejection performance depends on jet radius within the same p_T bin. To within 40%, the background rejection power of the groomed masses remains constant with respect to the jet radius. However, we again see rather different behaviour for the substructure variables. In all p_T bins considered the most performant substructure variable, $C_2^{\beta=1}$, performs best for an anti-k_{T} distance parameter of R=0.8. The performance of this variable is dramatically worse for the larger jet radius of R=1.2 (more than an order of magnitude worse background rejection in the 1.0-1.2 TeV bin), and substantially worse for R=0.4. For the other jet substructure variables considered, their background rejection power also reduces for larger jet radius. *Insert some nice discussion/explanation of why jet substructure power generally gets worse as we go to large jet radius, but groomed mass performance does not.*

6.3 Combined Performance

The off-diagonal entries in Figures 13, 14 and 15 can be used to compare the performance of different BDT two-variable combinations, and see how this varies as a function of p_T and R. By comparing the background rejection achieved for the two-variable combinations to the background rejection of the "all variables" BDT, one can understand how much more discrimination is possible by adding further variables to the two-variable BDTs.

One can see that in general the most powerful two-variable combinations involve a groomed mass and a non-mass substructure variable ($C_2^{\beta=1}$, Γ_{Qjet} or $\tau_{21}^{\beta=1}$). Two-variable combinations of the substructure variables are not powerful in comparison. The background rejection of the most powerful mass + substructure combination comes very close to that achieved in the "all variables" case, indicating that there is little to be gained by making a BDT that is more complex, and that there is little more complementary information available, at least in terms of that which is offered by the variables considered here.

One can also see that there is a modest improvement in the background rejection when different groomed masses are combined, compared to the single variable groomed mass performance, indicating that there is complementary information between the different groomed masses. There is also an improvement in the background rejection when the groomed masses are combined with

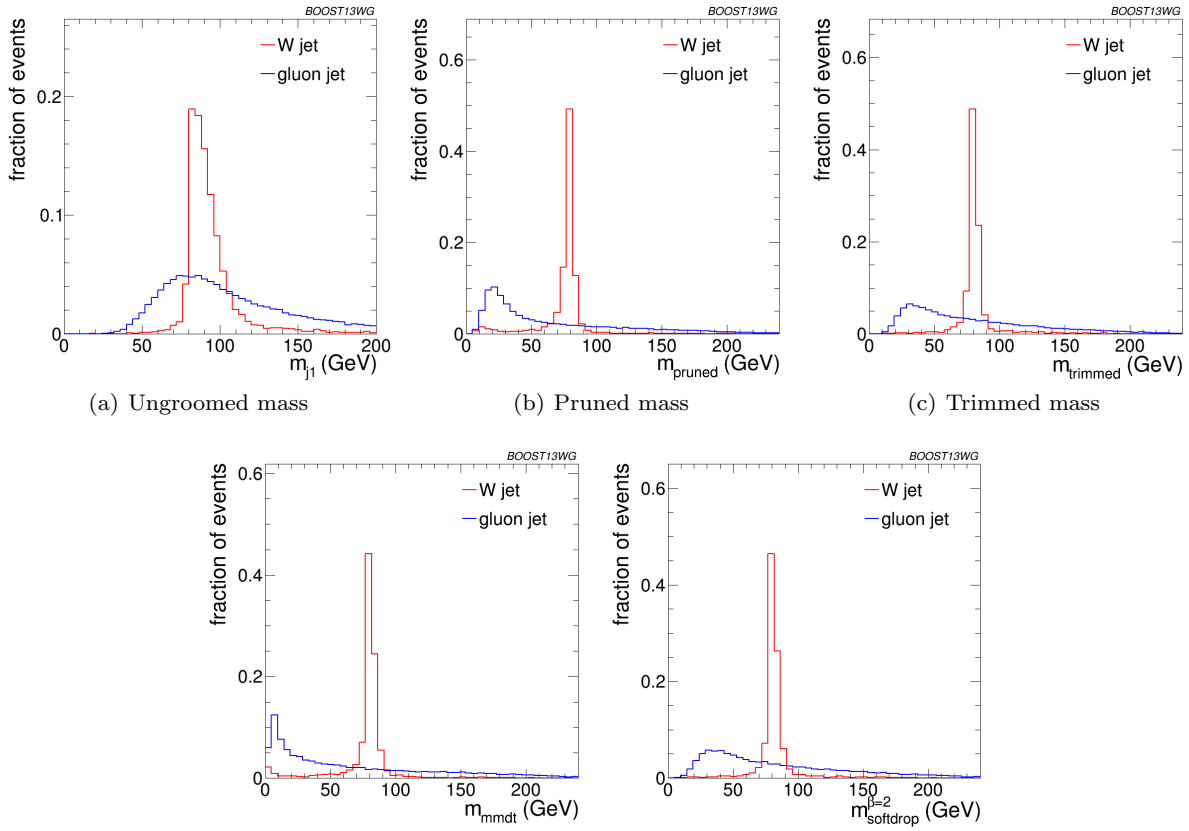

(a) Ungroomed mass (b) Pruned mass (c) Trimmed mass

(d) mMDT mass (e) Soft-drop $\beta = 2$ mass

Fig. 8 Comparisons of the QCD background to the WW signal in the p_T 500-650 GeV bin using the anti-k_T R=0.8 algorithm: leading jet mass distributions.

the ungroomed mass, indicating that grooming removes some useful discriminatory information from the jet.

6.3.1 Dependence on p_T

6.3.2 Dependence on R

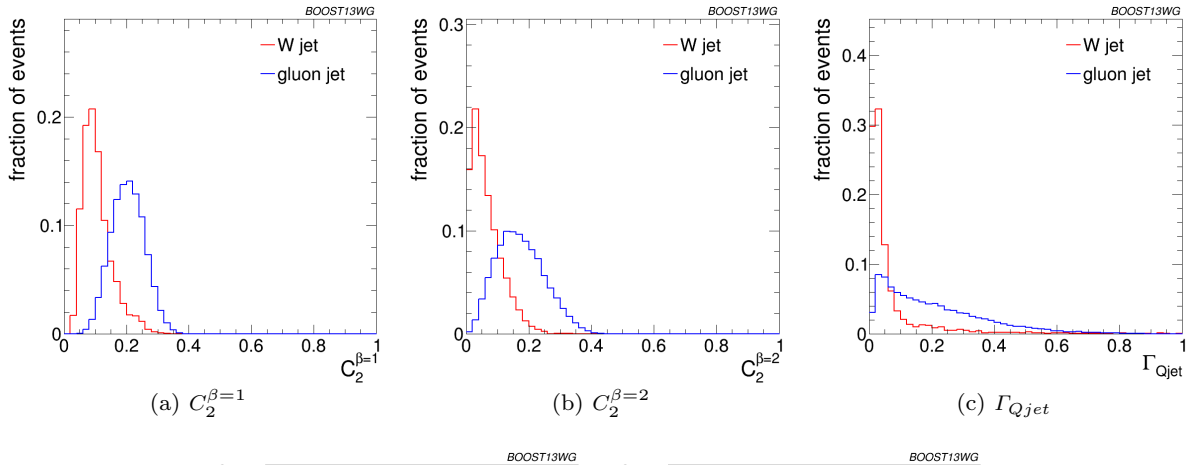

(a) $C_2^{\beta=1}$ (b) $C_2^{\beta=2}$ (c) Γ_{Qjet}

(d) $\tau_{21}^{\beta=1}$ (e) $\tau_{21}^{\beta=2}$

Fig. 9 Comparisons of the QCD background to the WW signal in the p_T 500-650 GeV bin using the anti-k_T R=0.8 algorithm: substructure variables.

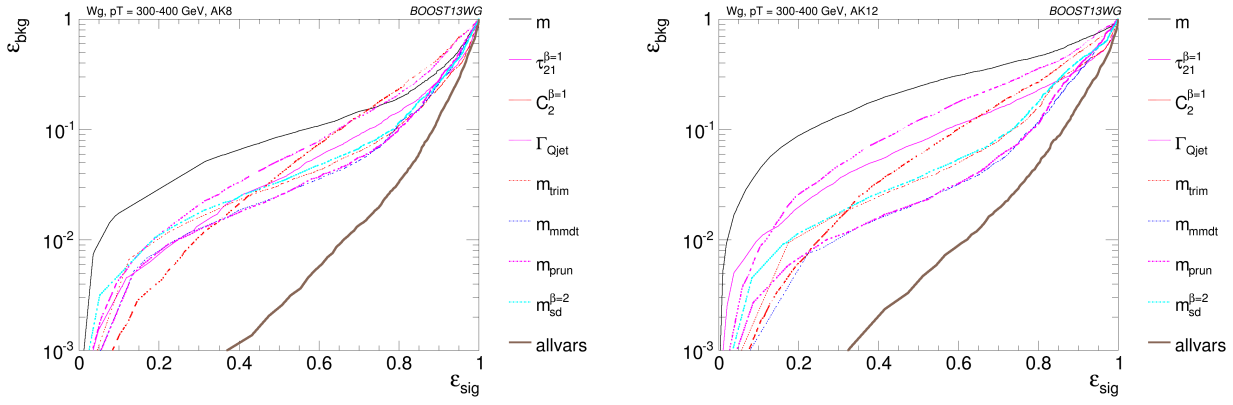

(a) anti-k_T R=0.8, p_T 300-450 GeV bin (b) anti-k_T R=1.2, p_T 300-450 GeV bin

Fig. 10 The ROC curve for all single variables considered for W tagging in the p_T 300-450 GeV bin using the anti-k_T R=0.8 algorithm and R=1.2 algorithm.

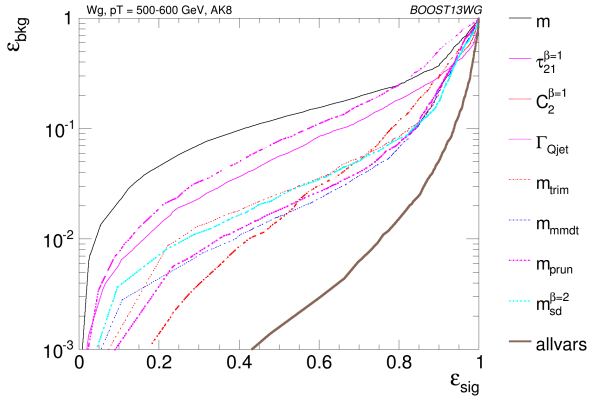

(a) anti-k_T R=0.8, p_T 500-650 GeV bin

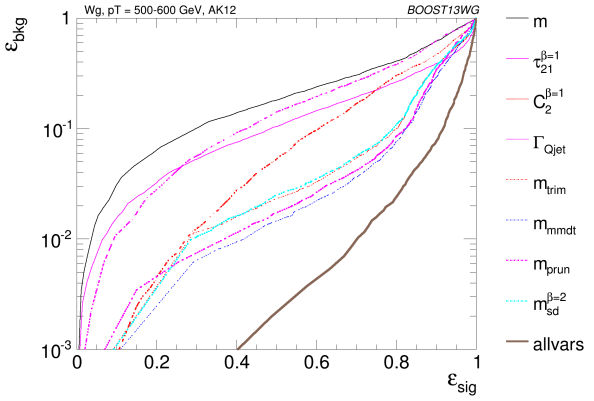

(b) anti-k_T R=1.2, p_T 500-650 GeV bin

Fig. 11 The ROC curve for all single variables considered for W tagging in the p_T 500-650 GeV bin using the anti-k_T R=0.8 algorithm and R=1.2 algorithm.

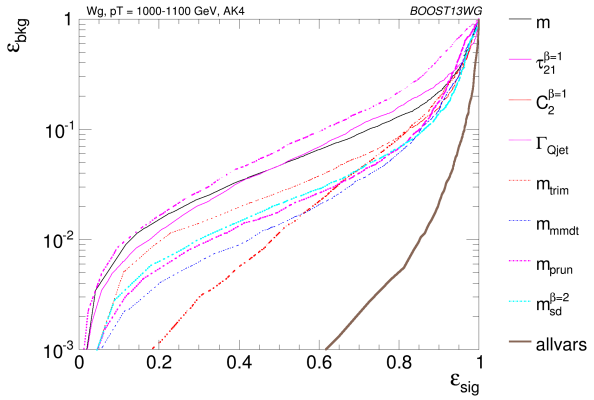

(a) anti-k_T R=0.4, p_T 1.0-1.2 TeV bin

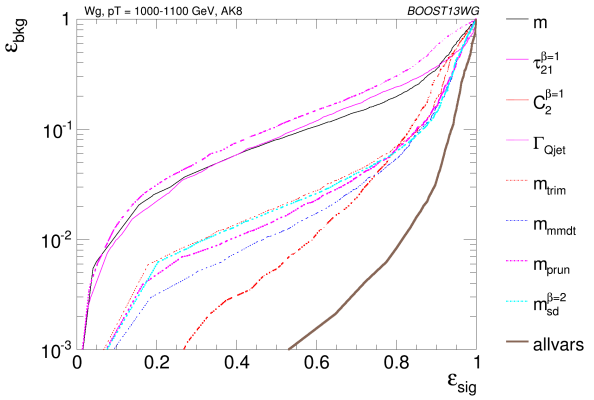

(b) anti-k_T R=0.8, p_T 1.0-1.2 TeV bin

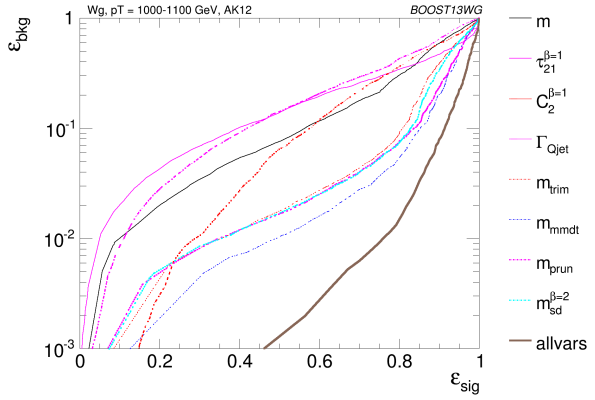

(c) anti-k_T R=1.2, p_T 1.0-1.2 TeV bin

Fig. 12 The ROC curve for all single variables considered for W tagging in the p_T 1.0-1.2 TeV bin using the anti-k_T R=0.4 algorithm, anti-k_T R=0.8 algorithm and R=1.2 algorithm.

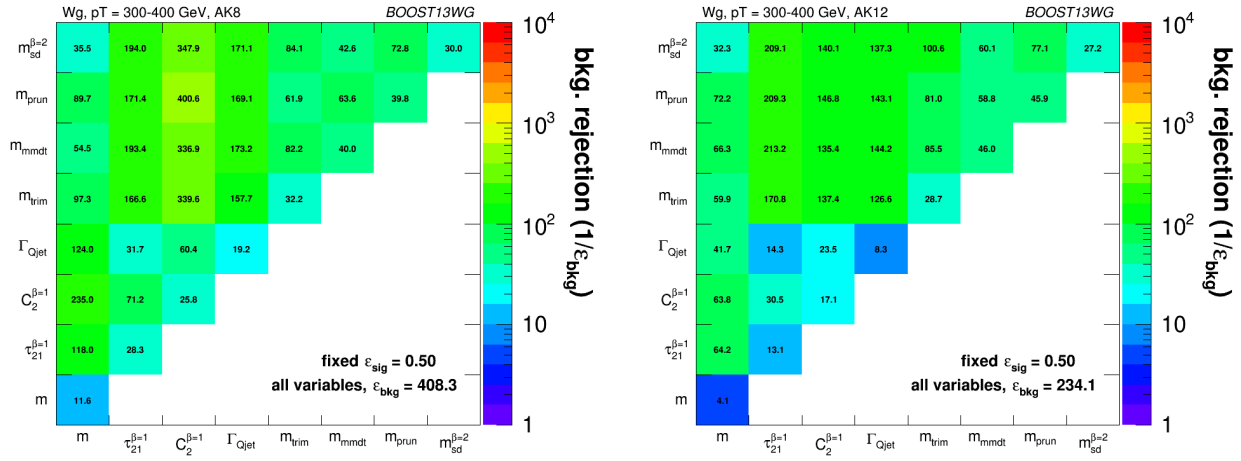

(a) anti-k_T R=0.8, p_T 300-450 GeV bin (b) anti-k_T R=1.2, p_T 300-450 GeV bin

Fig. 13 The background rejection for a fixed signal efficiency (50%) of each BDT combination of each pair of variables considered, in the p_T 300-450 GeV bin using the anti-k_T R=0.8 algorithm and R=1.2 algorithm. Also shown is the background rejection for a BDT combination of all of the variables considered.

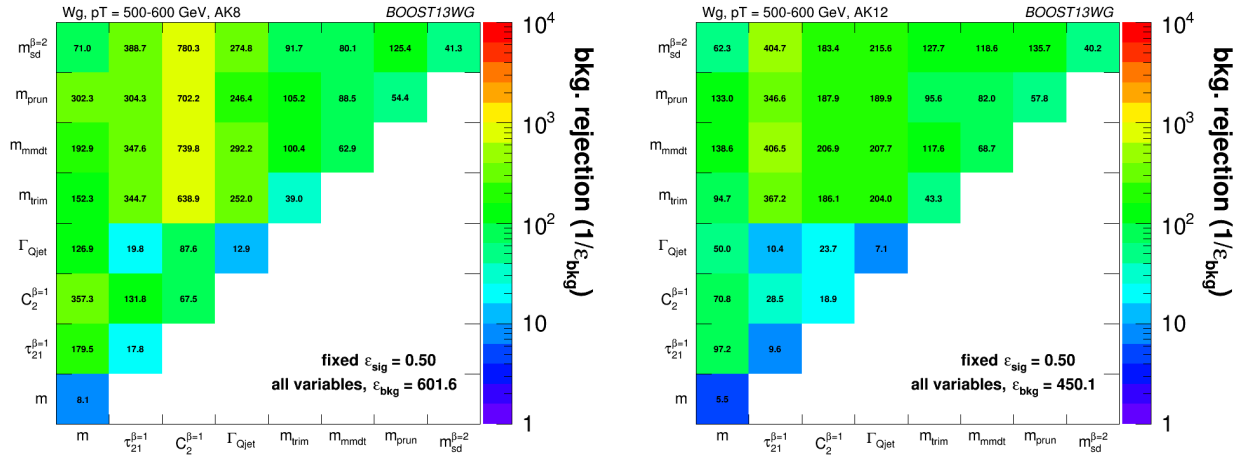

(a) anti-k_T R=0.8, p_T 500-650 GeV bin (b) anti-k_T R=1.2, p_T 500-650 GeV bin

Fig. 14 The background rejection for a fixed signal efficiency (50%) of each BDT combination of each pair of variables considered, in the p_T 500-650 GeV bin using the anti-k_T R=0.8 algorithm and R=1.2 algorithm. Also shown is the background rejection for a BDT combination of all of the variables considered.

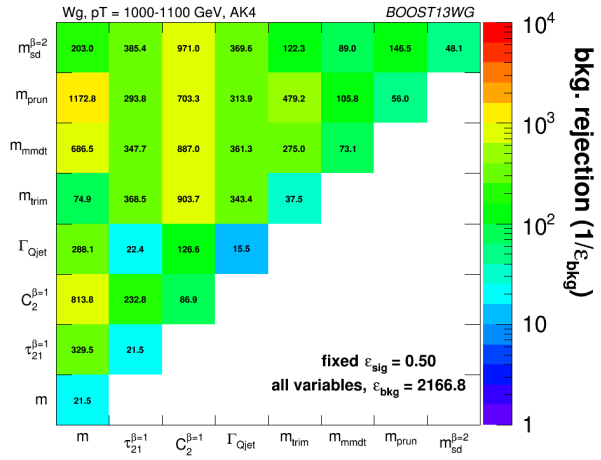

(a) anti-k_{T} R=0.4, p_T 1.0-1.2 TeV bin

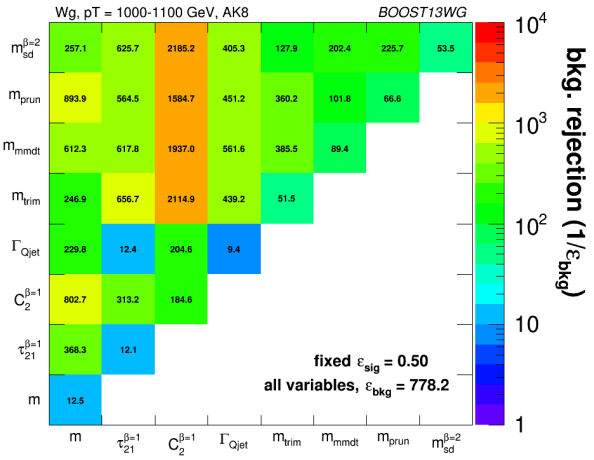

(b) anti-k_{T} R=0.8, p_T 1.0-1.2 TeV bin

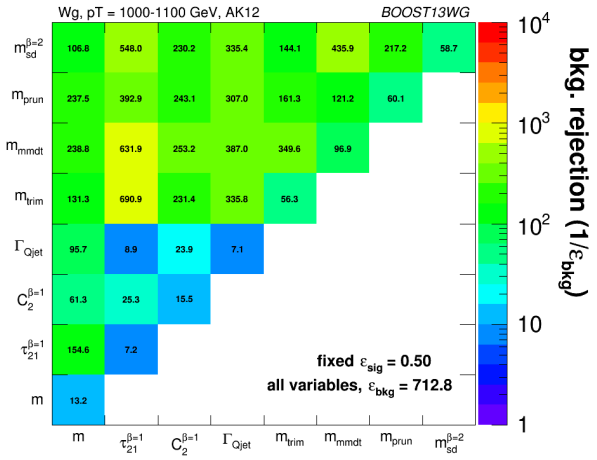

(c) anti-k_{T} R=1.2, p_T 1.0-1.2 TeV bin

Fig. 15 The background rejection for a fixed signal efficiency (50%) of each BDT combination of each pair of variables considered, in the p_T 1.0-1.2 TeV bin using the anti-k_{T} R=0.4, R=0.8 and R=1.2 algorithm. Also shown is the background rejection for a BDT combination of all of the variables considered.

7 Top Tagging

In this section, we study the identification of boosted top quarks at Run II of the LHC. Boosted top quarks result in large-radius jets with complex substructure, containing a b-subjet and a boosted W. The additional kinematic handles coming from the reconstruction of the W mass and b-tagging allows a very high degree of discrimination of top quark jets from QCD backgrounds.

We consider top quarks with moderate boost (600-1000 GeV), and perhaps most interestingly, at high boost ($\gtrsim$ 1500 GeV). Top tagging faces several challenges in the high-p_T regime. For such high-p_T jets, the b-tagging efficiencies are no longer reliably known. Also, the top jet can also accompanied by additional radiation with $p_T \sim m_t$, leading to combinatoric ambiguities of reconstructing the top and W, and the possibility that existing taggers or observables shape the background by looking for subjet combinations that reconstruct m_t/m_W. To study this, we examine the performance of both mass-reconstruction variables, as well as shape observables that probe the three-pronged nature of the top jet and the accompanying radiation pattern.

7.1 Methodology

We study a number of top-tagging strategies, in particular:

1. HEPTopTagger
2. Johns Hopkins Tagger (JH)
3. Trimming
4. Pruning

The top taggers have criteria for reconstructing a top and W candidate, while the grooming algorithms (trimming and pruning) do not incorporate a W-identification step. For a level playing field, we construct a W candidate from the three leading subjets by taking the pair of subjets with the smallest invariant mass; in the case that only two subjets are reconstructed, we take the mass of the leading subjet. All of the above taggers and groomers incorporate a step to remove pile-up and other soft radiation.

We also consider the performance of jet shape observables. In particular, we consider the N-subjettiness ratios $\tau_{32}^{\beta=1}$ and $\tau_{21}^{\beta=1}$, energy correlation function ratios $C_3^{\beta=1}$ and $C_2^{\beta=1}$, and the Qjet mass volatility Γ. In addition to the jet shape performance, we combine the jet shapes with the mass-reconstruction methods listed above to determine the optimal combined performance.

To quantify the performance of each set of variables, we combine the relevant tagger output observables and/or jet shapes into a boosted decision tree (BDT), which determines the optimal multivariable cut. Additionally, because each tagger has two inputs (list, or maybe refer back to Section 3), we scan over reasonable values of the inputs to determine the optimal value for each top tagging signal efficiency. This allows a direct comparison of the optimized version of each tagger. The input values scanned for the various algorithms are:

- **HEPTopTagger:** $m \in [30, 100]$ GeV, $\mu \in [0.5, 1]$
- **JH Tagger:** $\delta_p \in [0.02, 0.15]$, $\delta_R \in [0.07, 0.2]$
- **Trimming:** $f_{\rm cut} \in [0.02, 0.14]$, $R_{\rm trim} \in [0.1, 0.5]$
- **Pruning:** $z_{\rm cut} \in [0.02, 0.14]$, $R_{\rm cut} \in [0.1, 0.6]$

7.2 Single-observable performance

We start by investigating the behavior of individual jet substructure observables. Because of the rich, three-pronged structure of the top decay, it is expected that combinations of masses and jet shapes will far out-perform single observables in identifying boosted tops. However, a study of the top-tagging performance of single variables facilitates a direct comparison with the W tagging results in Section 6, and also allows a straightforward examination of the performance of each observable for different p_T and jet radius.

Fig. 16 shows the ROC curves for each of the top-tagging observables, with the bare jet mass also plotted for comparison. Unlike W tagging, the jet shape observables perform more poorly than jet mass. *(Check reasoning: this argument due to Andrew Larkoski).* As an example illustrating why this is the case, consider N-subjettiness. The W is two-pronged and the top is three-pronged; therefore, we expect τ_{21} and τ_{32} to be the best-performant N-subjettiness ratio, respectively. However, τ_{21} also contains an implicit cut on the denominator, τ_1, which is strongly correlated with jet mass. Therefore, τ_{21} combines both mass and shape information to some extent. By contrast, and as is clear in Fig.16(a), the best shape for top tagging is τ_{32}, which contains no information on the mass. Therefore, it is unsurprising that the shapes most useful for top tagging are less sensitive to the jet mass, and under-perform relative to the corresponding observables for W tagging.

Of the two top tagging algorithms, the Johns Hopkins (JH) tagger out-performs the HEPTopTagger in its signal-to-background separation of both the top and W candidate masses, with larger discrepancy at higher p_T and larger jet radius. In Fig. 17, we show the histograms for the top mass output from the JH and HEPTopTagger for different p_T and R, optimized at a signal efficiency of 30%. The likely reason for this behavior is that, in the HEPTopTagger algorithm, the jet is filtered to select the five hardest subjets, and then three subjets are chosen which reconstruct the top mass. This requirement tends to shape a peak in the QCD background around m_t for the HEPTopTagger, while the JH tagger has no such requirement. It has been suggested by Anders *et al.* [**?**] that performance in the HEPTopTagger may be improved by selecting the three subjets reconstructing the top only among those that pass the W mass constraints, which somewhat reduces the shaping of the background. Note that both the JH tagger and the HEPTopTagger are superior at using the W candidate inside of the top for signal discrimination; this is because the the pruning and trimming algorithms do not have inherent W-identification steps and are not optimized for this purpose.

We also directly compare the performance of top mass and jet shape observables for different jet p_T and radius. The results are shown in Figs. 19-20 for different p_T bins and Figs. 21-22 for different R values. The input parameters of the taggers, groomers, and shape variables are separately optimized for each p_T and radius.

p_T comparison: We compare various top tagging observables for jets in different p_T bins and $R = 0.8$. The tagging performance of jet shapes do not change substantially with p_T. $\tau_{32}^{(\beta=1)}$ and the Qjet volatility Γ have the most variation and tend to degrade with higher p_T. This makes sense, as higher-p_T QCD jets have more, harder emissions within the jet, giving rise to substructure that fakes the signal. By contrast, most of the top mass observables have superior performance at higher p_T due to the radiation from the top quark becoming more collimated. The notable exception is the HEPTopTagger, which degrades at higher p_T, likely in part due to the background-shaping effects discussed earlier.

R comparison: We compare various top tagging observables for jets of different R and $p_T = 1.5 - 1.6$ TeV. Most of the top-tagging parameters perform best for smaller radius; this is because, at such high p_T, most of the radiation from the top quark is confined within $R = 0.4$, and having a larger jet radius makes the observable more susceptible to contamination from the underlying event and other uncorrelated radiation. The main exception is $C_3^{(\beta=1)}$, which performs optimally at $R = 0.8$. *why?*

7.3 Performance of multivariable combinations

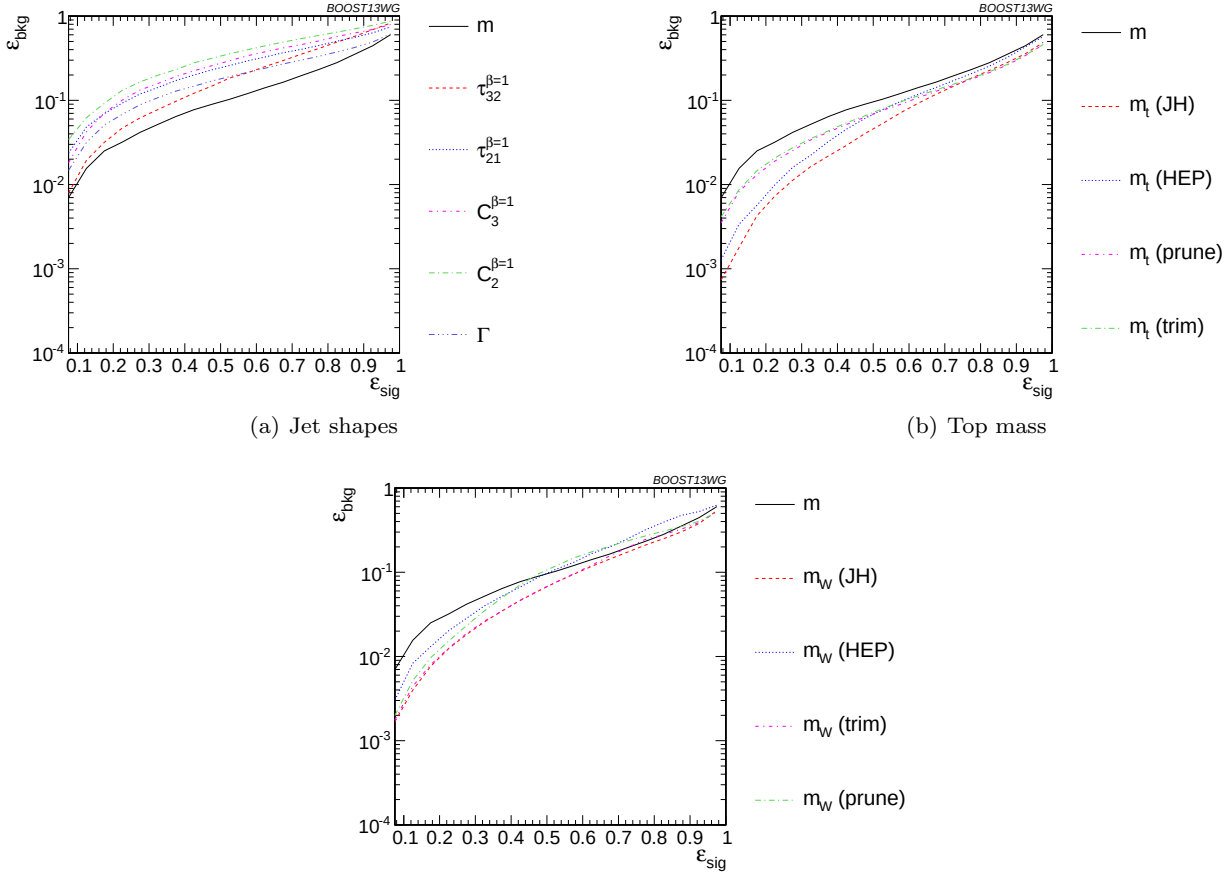

(a) Jet shapes

(b) Top mass

(c) W mass

Fig. 16 Comparison of single-variable top-tagging performance in the p_T 1000-1100 GeV bin using the anti-k_{T}, R=0.8 algorithm.

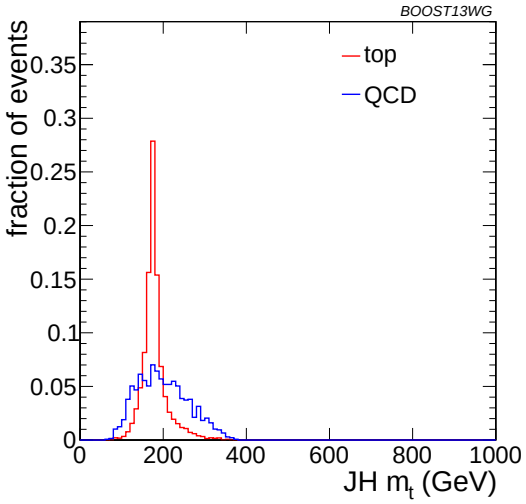

(a) Johns Hopkins Tagger, $R = 0.4$

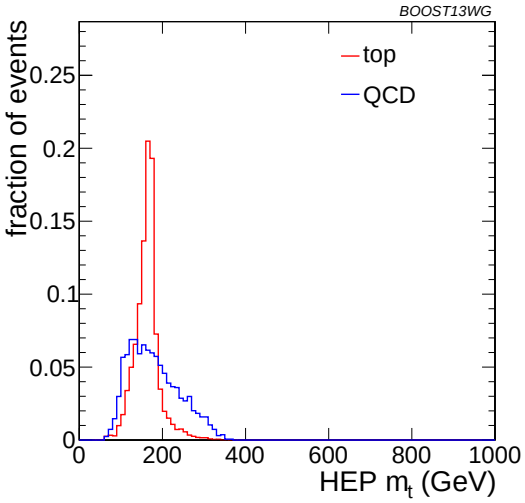

(b) HEPTopTagger, $R = 0.4$

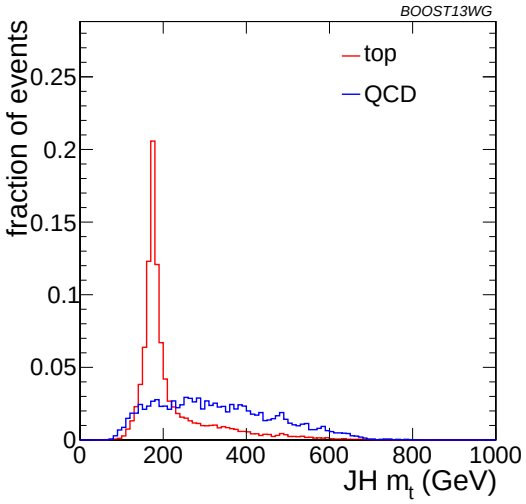

(c) Johns Hopkins Tagger, $R = 0.8$

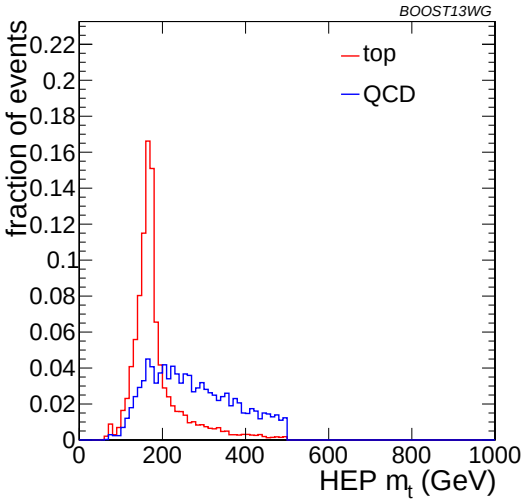

(d) HEPTopTagger, $R = 0.8$

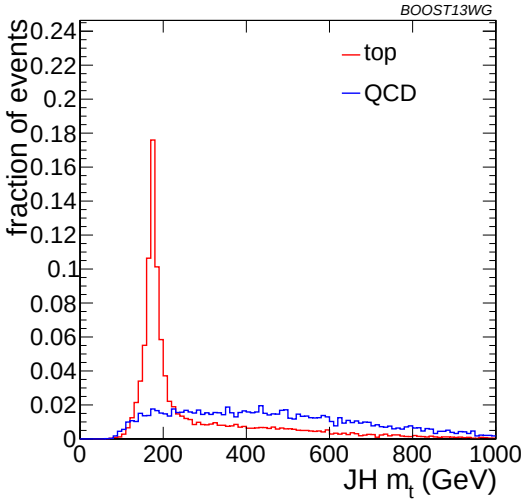

(e) Johns Hopkins Tagger, $R = 1.2$

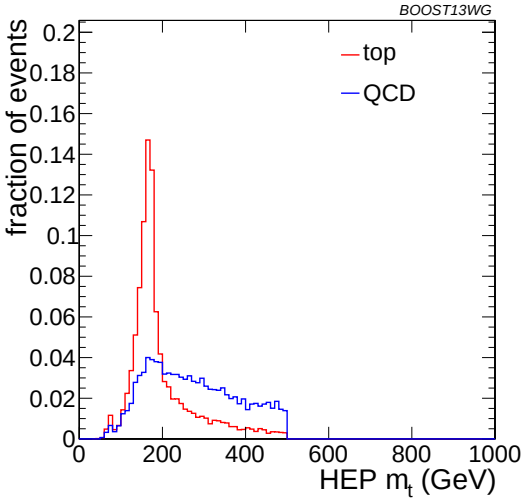

(f) HEPTopTagger, $R = 1.2$

Fig. 17 Comparison of top mass reconstruction with the JH and HEPTopTaggers at different R using the anti-k_{T} algorithm, $p_{\mathrm{T}} = 1.5 - 1.6$ TeV. Each histogram is shown for the working point optimized for best performance with m_t at signal efficiency 0.3 and is normalized to the fraction of events passing the tagger.

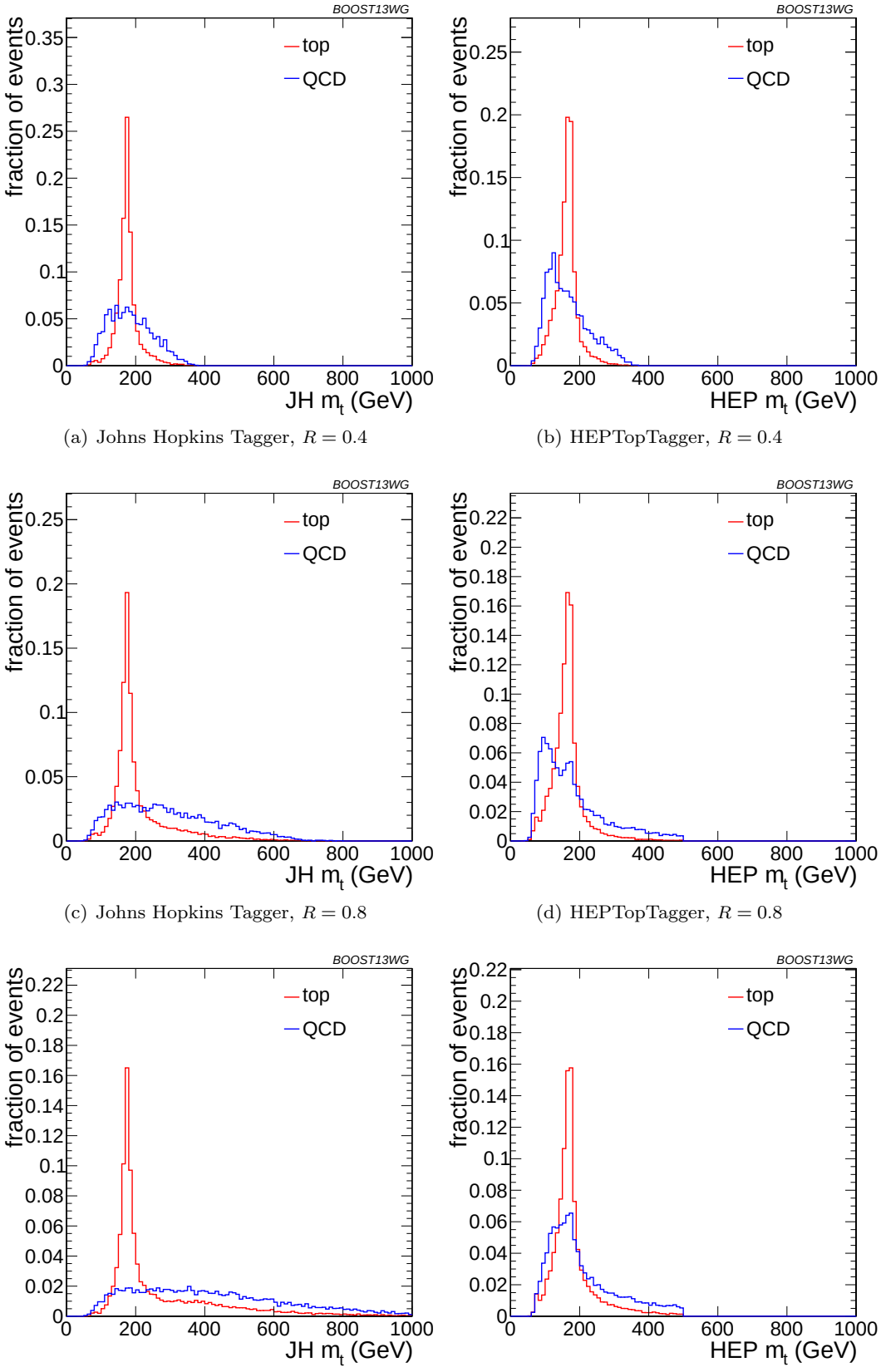

(a) Johns Hopkins Tagger, $R = 0.4$

(b) HEPTopTagger, $R = 0.4$

(c) Johns Hopkins Tagger, $R = 0.8$

(d) HEPTopTagger, $R = 0.8$

(e) Johns Hopkins Tagger, $R = 1.2$

(f) HEPTopTagger, $R = 1.2$

Fig. 18 Comparison of top mass reconstruction with the JH and HEPTopTaggers at different R using the anti-k_{T} algorithm, $p_{\mathrm{T}} = 1.5 - 1.6$ TeV. Each histogram is shown for the working point optimized for best performance of the tagger at signal efficiency 0.3 and is normalized to the fraction of events passing the tagger.

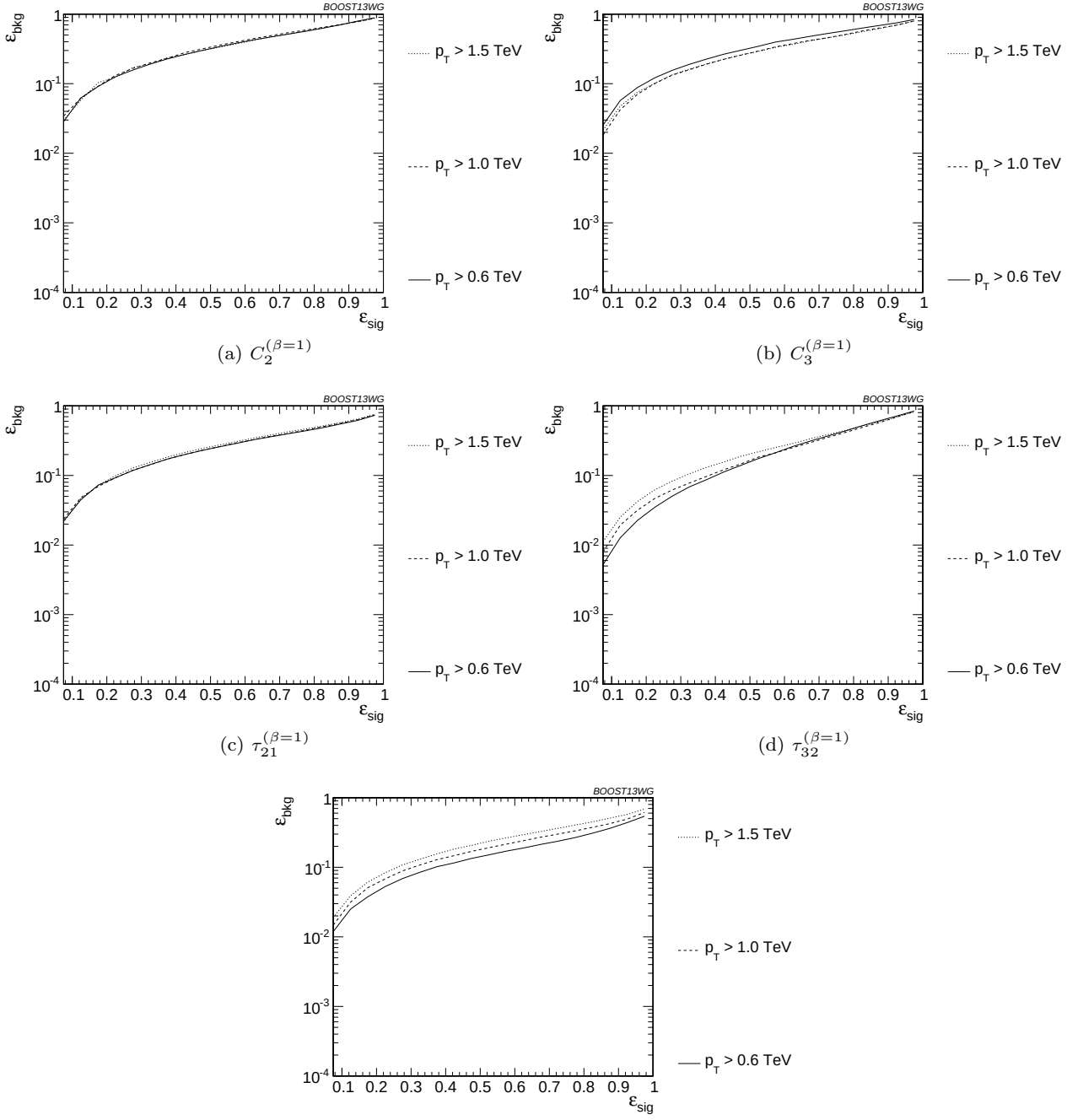

(a) $C_2^{(\beta=1)}$ (b) $C_3^{(\beta=1)}$

(c) $\tau_{21}^{(\beta=1)}$ (d) $\tau_{32}^{(\beta=1)}$

(e) Qjet mass volatility

Fig. 19 Comparison of individual jet shape performance at different p_T using the anti-k_{T} R=0.8 algorithm.

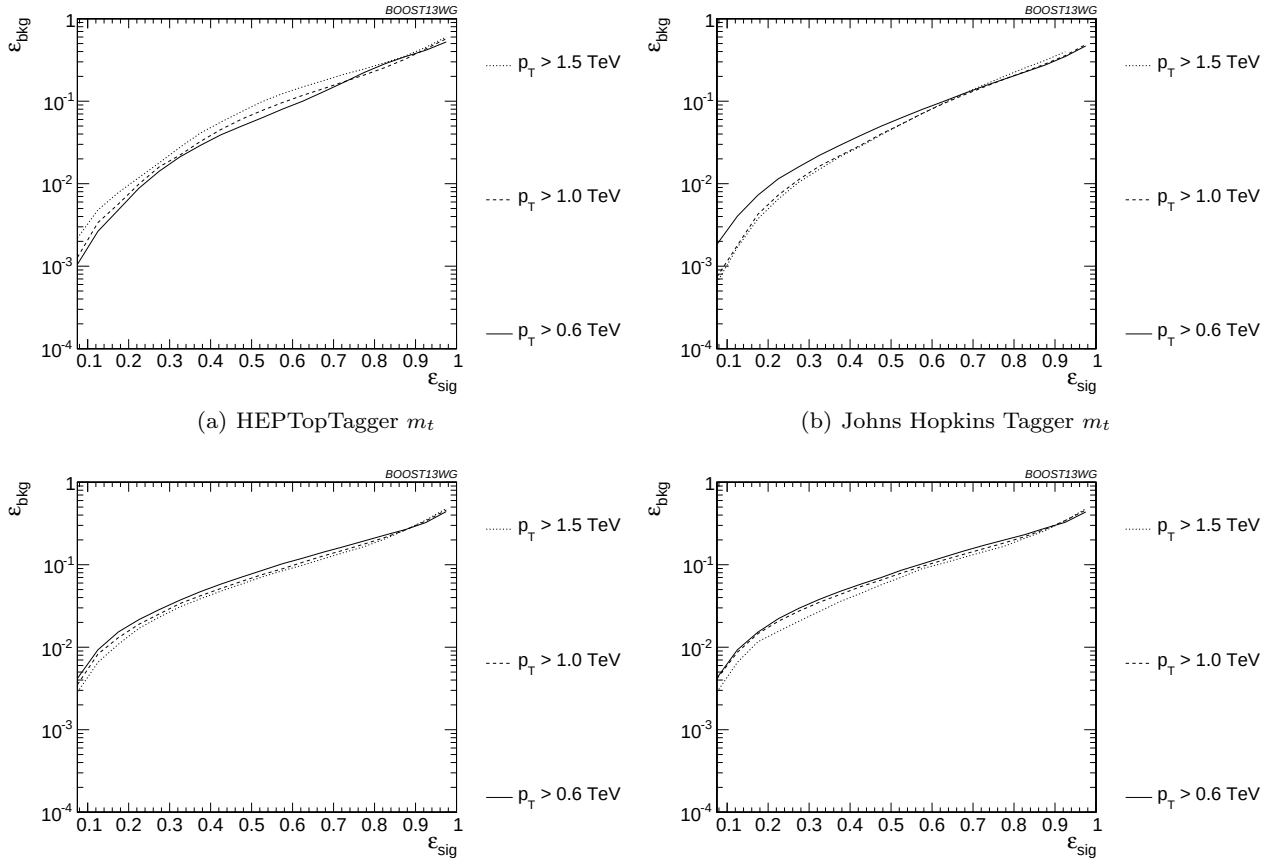

(a) HEPTopTagger m_t

(b) Johns Hopkins Tagger m_t

(c) Pruning m_t

(d) Trimming m_t

Fig. 20 Comparison of top mass performance of different taggers at different p_T using the anti-k_{T} R=0.8 algorithm.

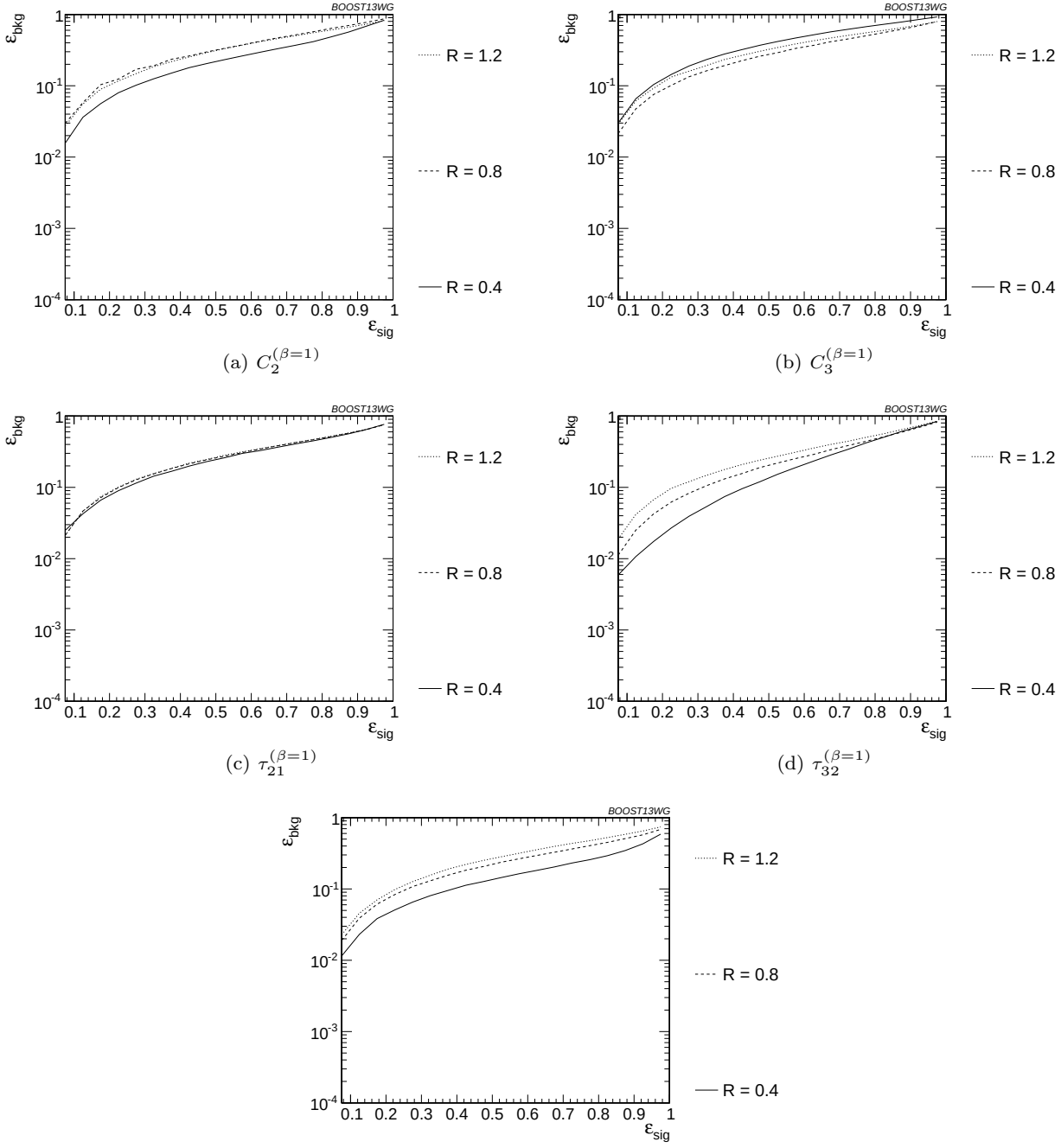

(a) $C_2^{(\beta=1)}$

(b) $C_3^{(\beta=1)}$

(c) $\tau_{21}^{(\beta=1)}$

(d) $\tau_{32}^{(\beta=1)}$

(e) Qjet mass volatility

Fig. 21 Comparison of individual jet shape performance at different R in the $p_T = 1500 - 1600$ GeV bin.

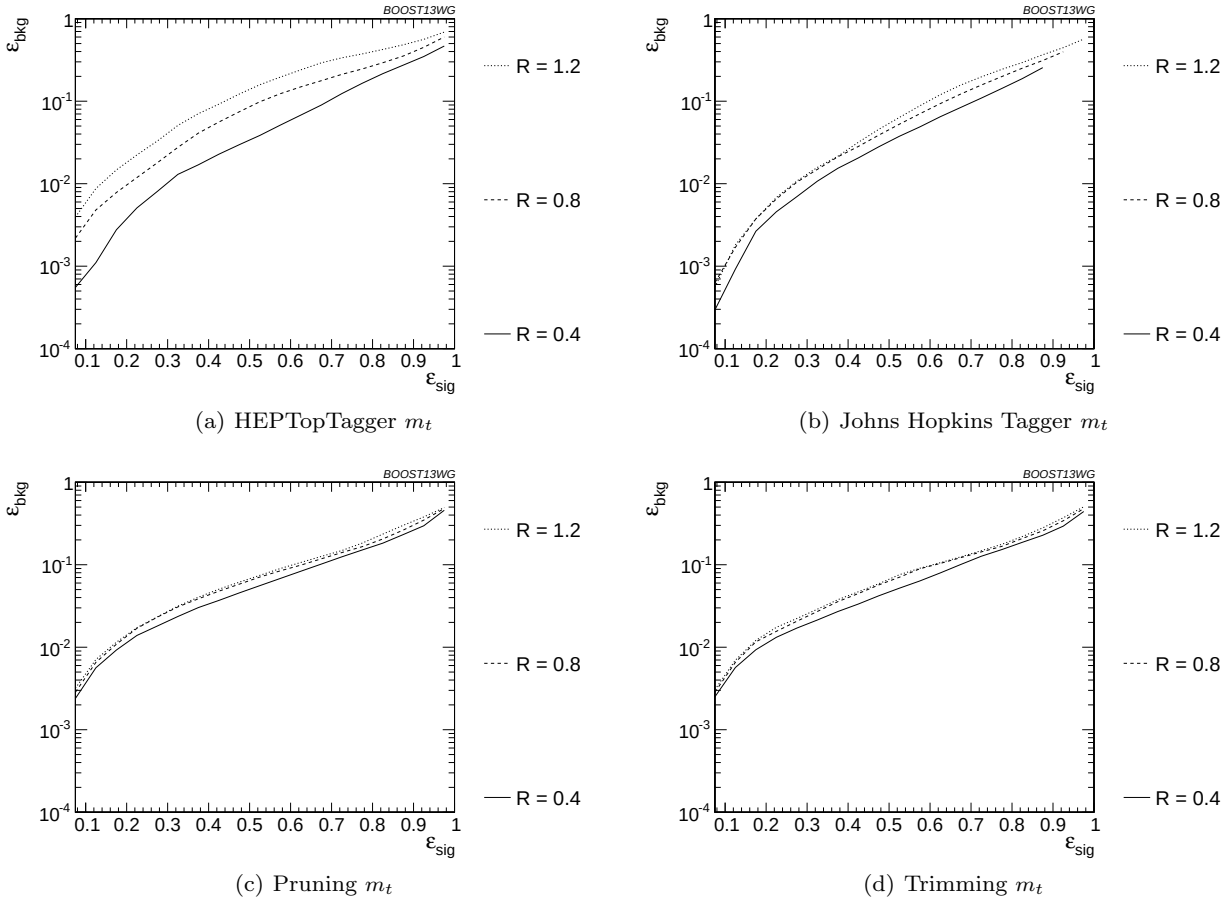

(a) HEPTopTagger m_t

(b) Johns Hopkins Tagger m_t

(c) Pruning m_t

(d) Trimming m_t

Fig. 22 Comparison of top mass performance of different taggers at different R in the $p_T = 1500 - 1600$ GeV bin.

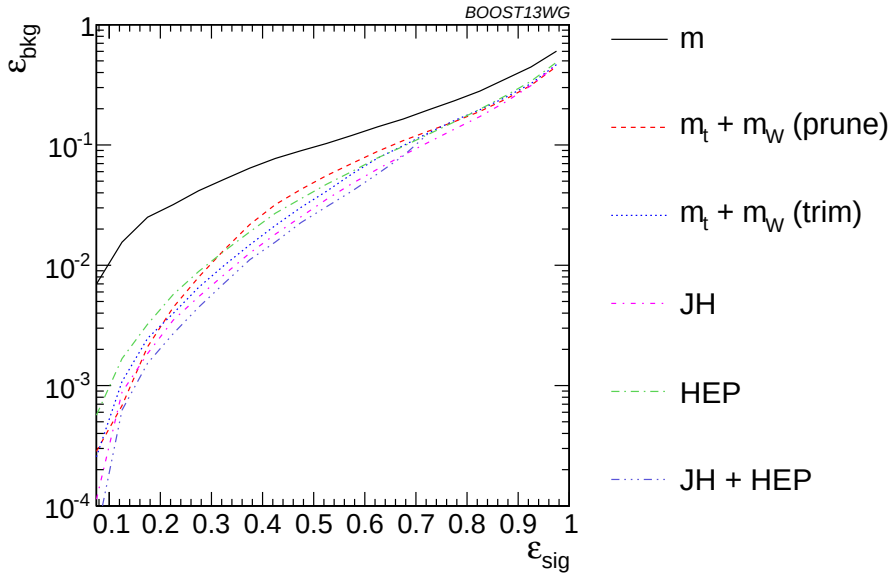

Fig. 23 Comparison of BDT combinations of each tagger output in the p_T 1000-1100 GeV bin using the anti-k_T R=0.8 algorithm.

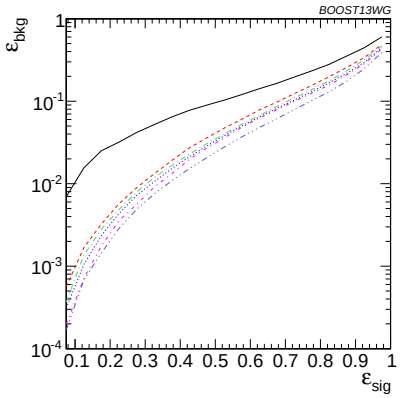

(a) HEPTopTagger

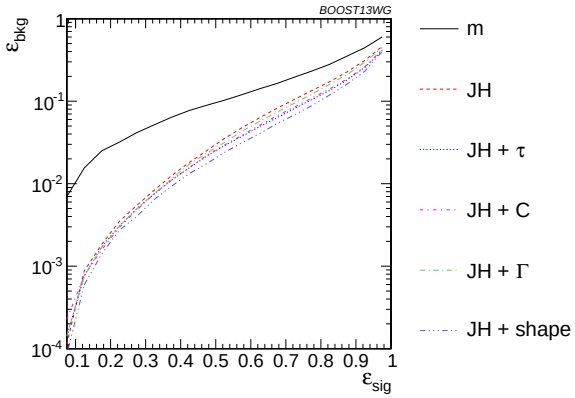

(b) Johns Hopkins Tagger

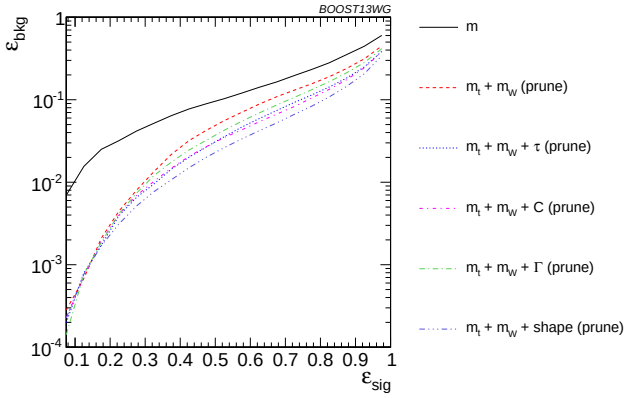

(c) Pruning

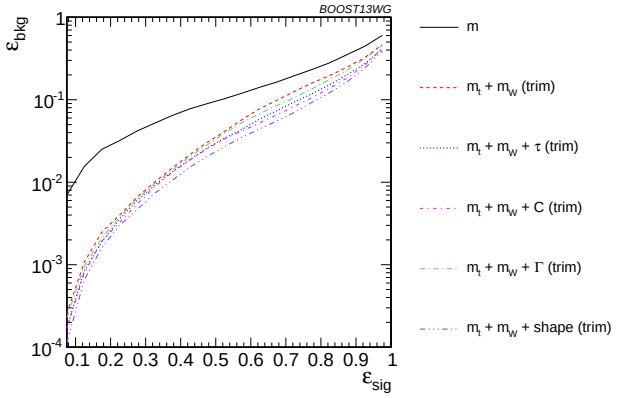

(d) Trimming

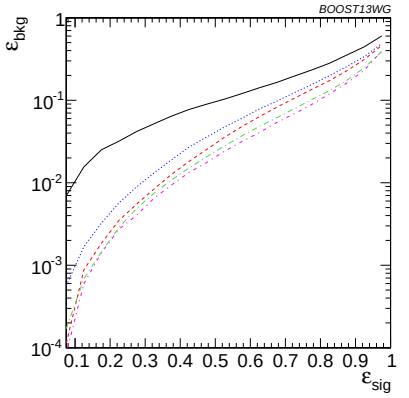

(e) HEP+JH comparison

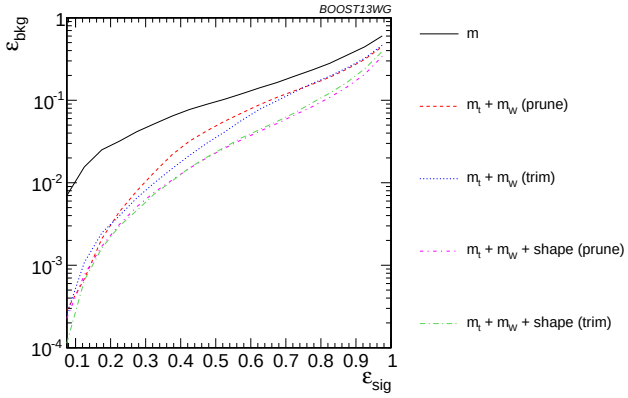

(f) Grooming comparison

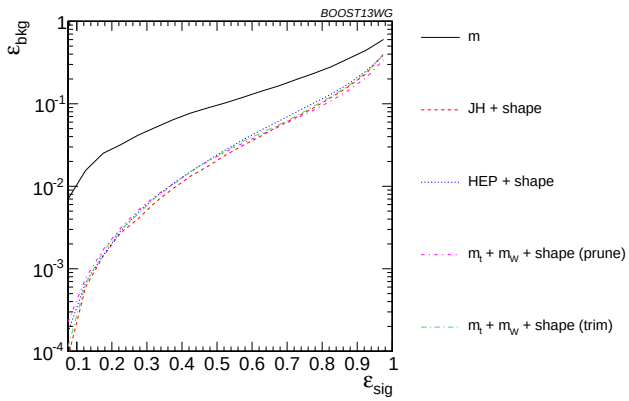

(g) Comparison of Tagger+Shape

Fig. 24 The BDT combinations in the p_T 1000-1100 GeV bin using the anti-k_T R=0.8 algorithm.

7.3.1 p_T comparison

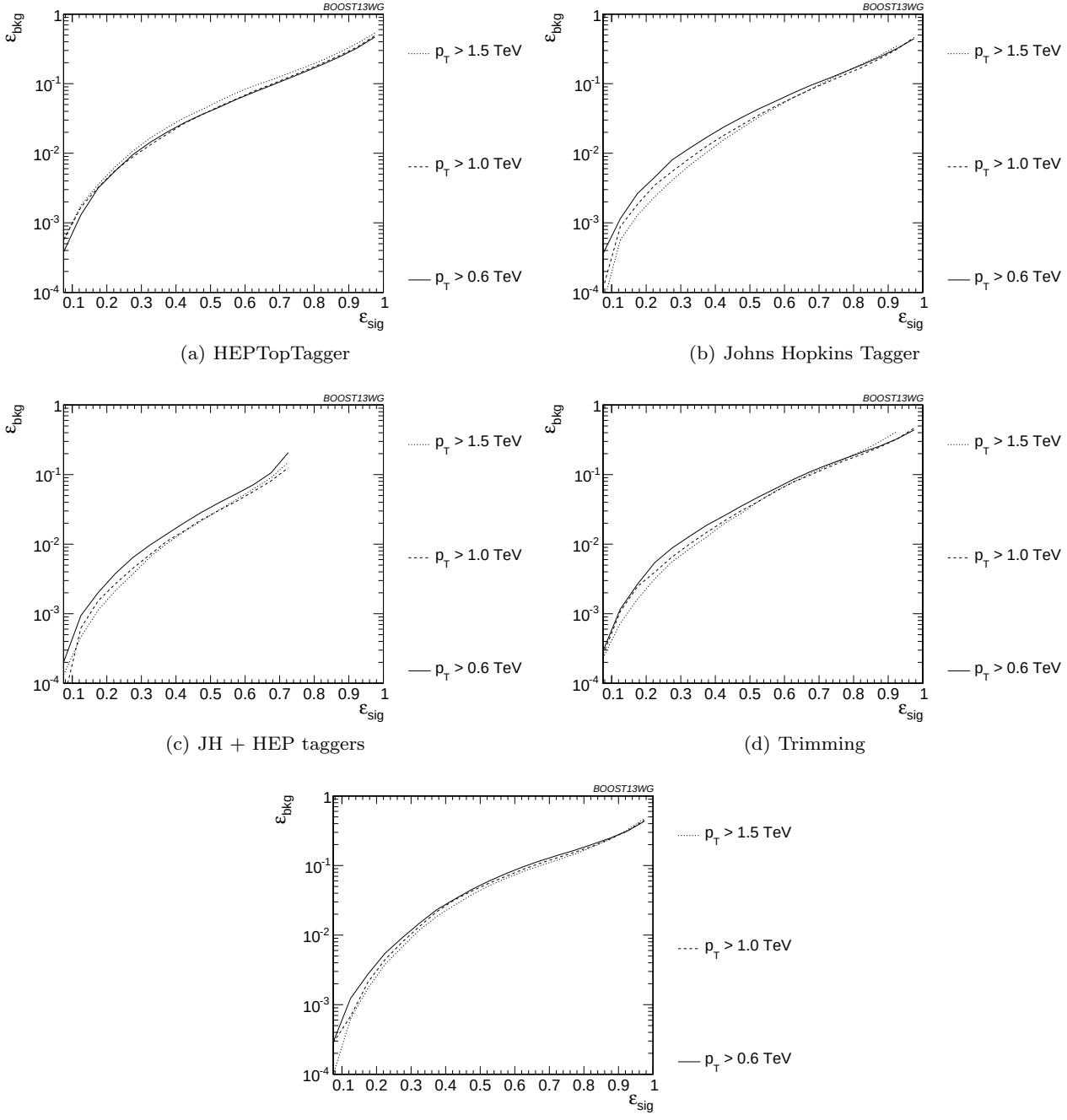

(a) HEPTopTagger

(b) Johns Hopkins Tagger

(c) JH + HEP taggers

(d) Trimming

(e) Pruning

Fig. 25 Comparison of BDT combination of tagger performance at different p_T using the anti-k_T R=0.8 algorithm.

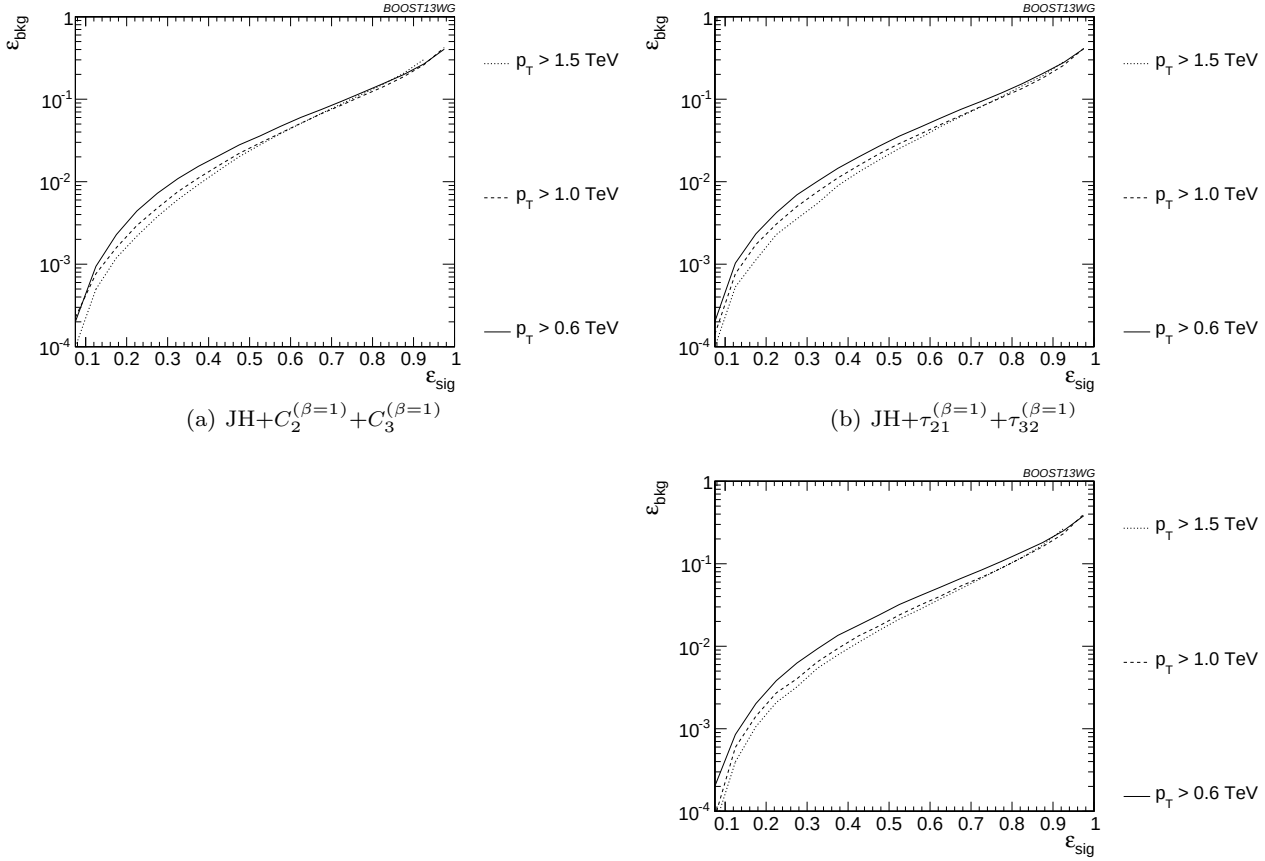

(a) JH+$C_2^{(\beta=1)}$+$C_3^{(\beta=1)}$

(b) JH+$\tau_{21}^{(\beta=1)}$+$\tau_{32}^{(\beta=1)}$

(c) JH + Qjet mass volatility

(d) JH + all

Fig. 26 Comparison of BDT combination of JH tagger + shape at different p_T using the anti-k_{T} R=0.8 algorithm.

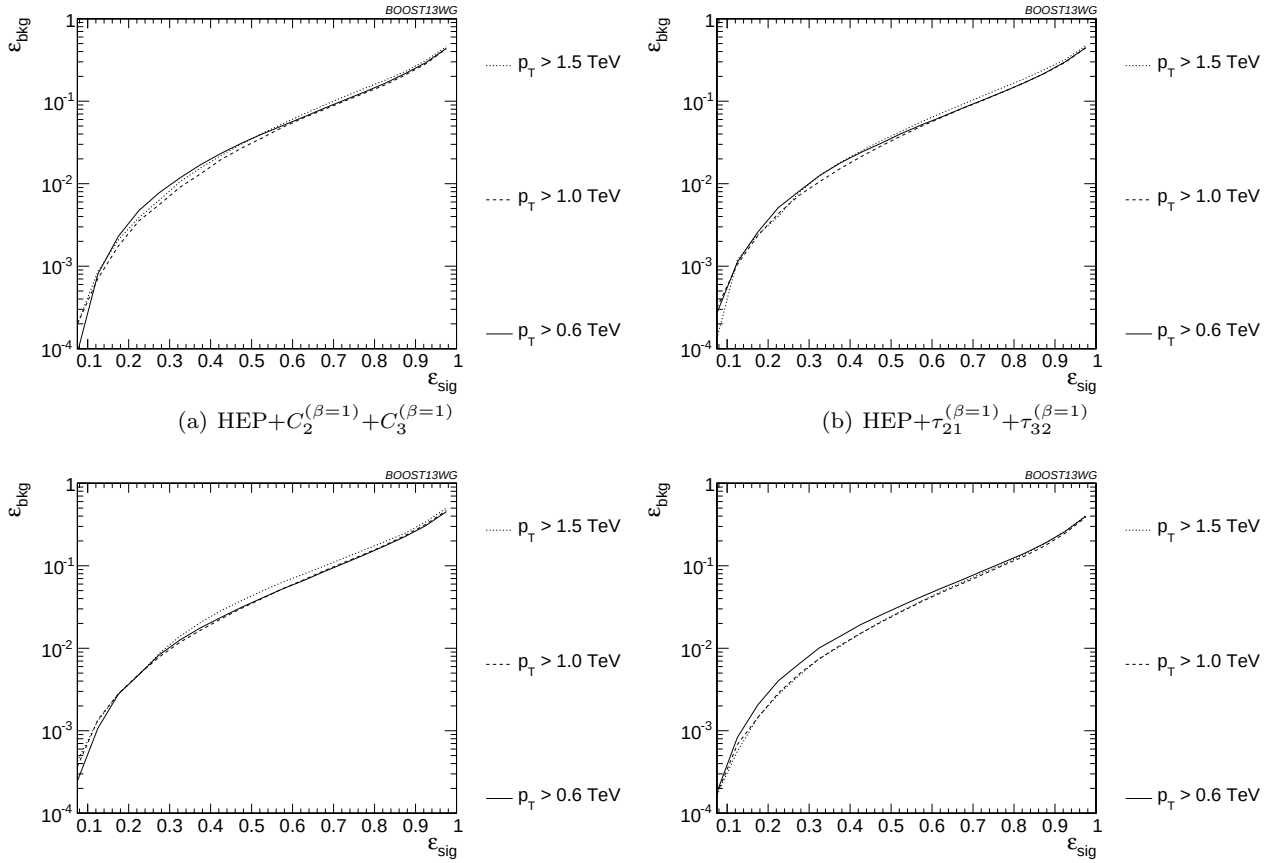

(a) HEP+$C_2^{(\beta=1)}$+$C_3^{(\beta=1)}$

(b) HEP+$\tau_{21}^{(\beta=1)}$+$\tau_{32}^{(\beta=1)}$

(c) HEP + Qjet mass volatility

(d) HEP + all

Fig. 27 Comparison of BDT combination of HEP tagger + shape at different p_T using the anti-k_{T} R=0.8 algorithm.

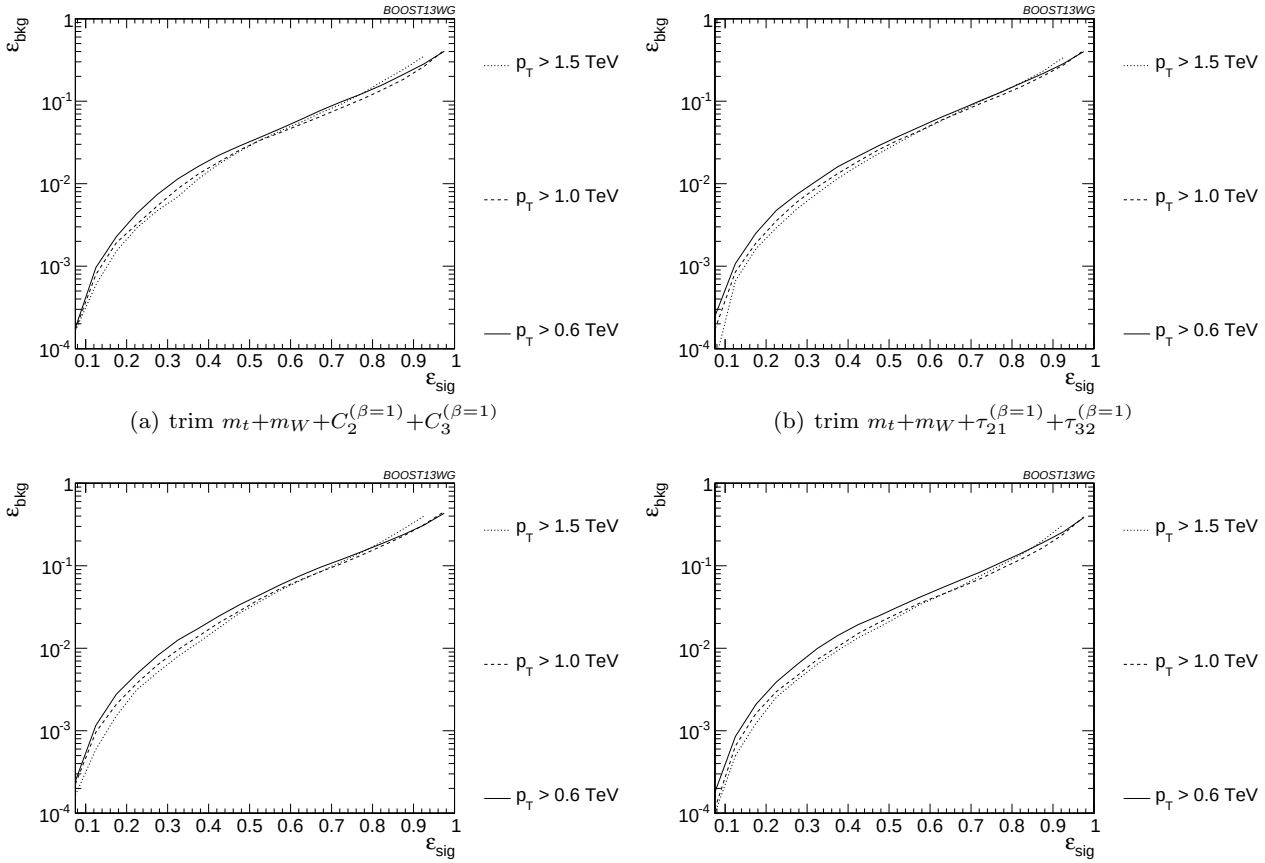

(a) trim m_t+m_W+$C_2^{(\beta=1)}$+$C_3^{(\beta=1)}$

(b) trim m_t+m_W+$\tau_{21}^{(\beta=1)}$+$\tau_{32}^{(\beta=1)}$

(c) trim m_t+m_W + Qjet mass volatility

(d) trim m_t+m_W + all

Fig. 28 Comparison of BDT combination of trimming + shape at different p_T using the anti-k_{T} R=0.8 algorithm.

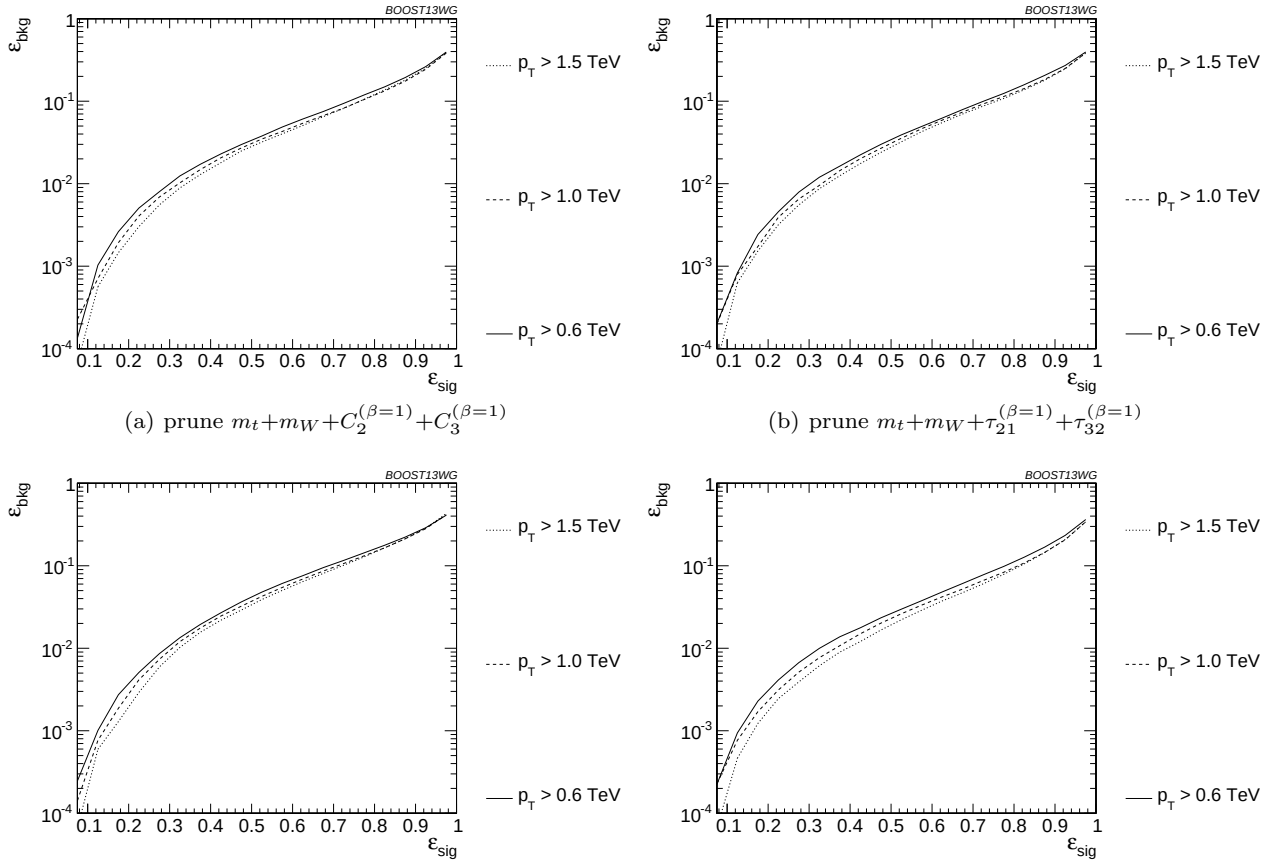

(a) prune m_t+m_W+$C_2^{(\beta=1)}$+$C_3^{(\beta=1)}$

(b) prune m_t+m_W+$\tau_{21}^{(\beta=1)}$+$\tau_{32}^{(\beta=1)}$

(c) prune m_t+m_W + Qjet mass volatility

(d) prune m_t+m_W + all

Fig. 29 Comparison of BDT combination of pruning + shape at different p_T using the anti-k_{T} R=0.8 algorithm.

7.3.2 R comparison

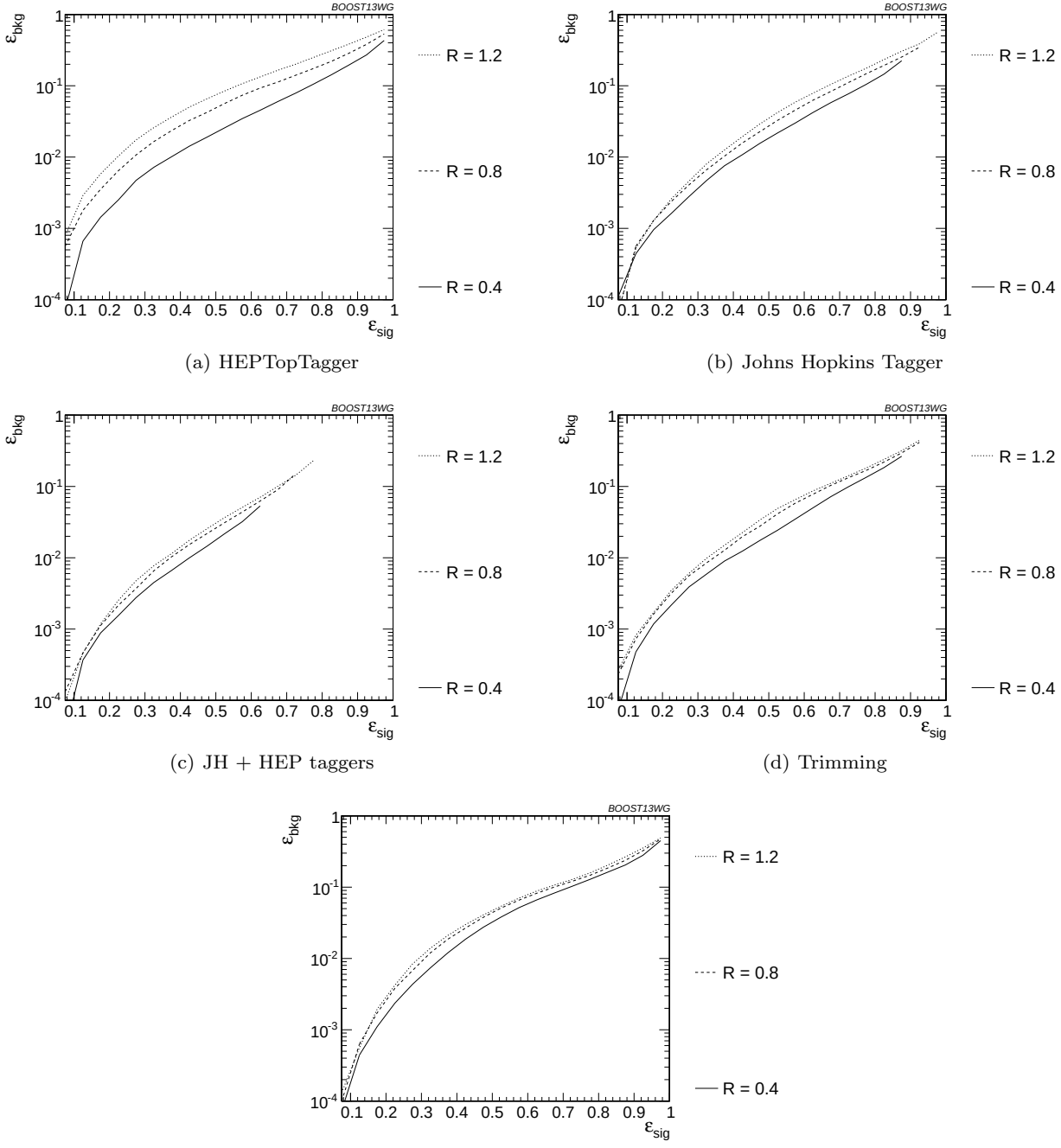

(a) HEPTopTagger

(b) Johns Hopkins Tagger

(c) JH + HEP taggers

(d) Trimming

(e) Pruning

Fig. 30 Comparison of tagger and jet shape performance at different radius at p_T = 1.5-1.6 TeV.

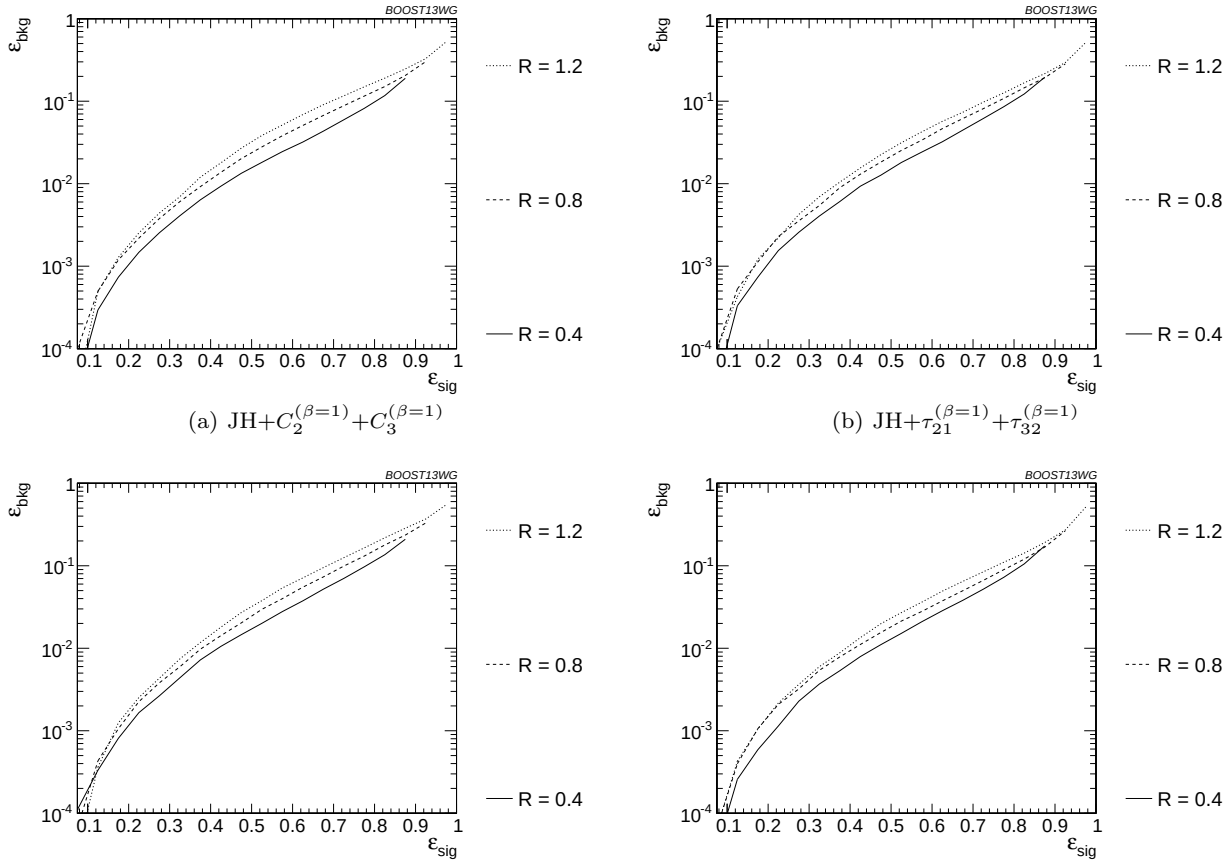

(a) JH+$C_2^{(\beta=1)}$+$C_3^{(\beta=1)}$

(b) JH+$\tau_{21}^{(\beta=1)}$+$\tau_{32}^{(\beta=1)}$

(c) JH + Qjet mass volatility

(d) JH + all

Fig. 31 Comparison of BDT combination of JH tagger + shape at different radius at p_T = 1.5-1.6 TeV.

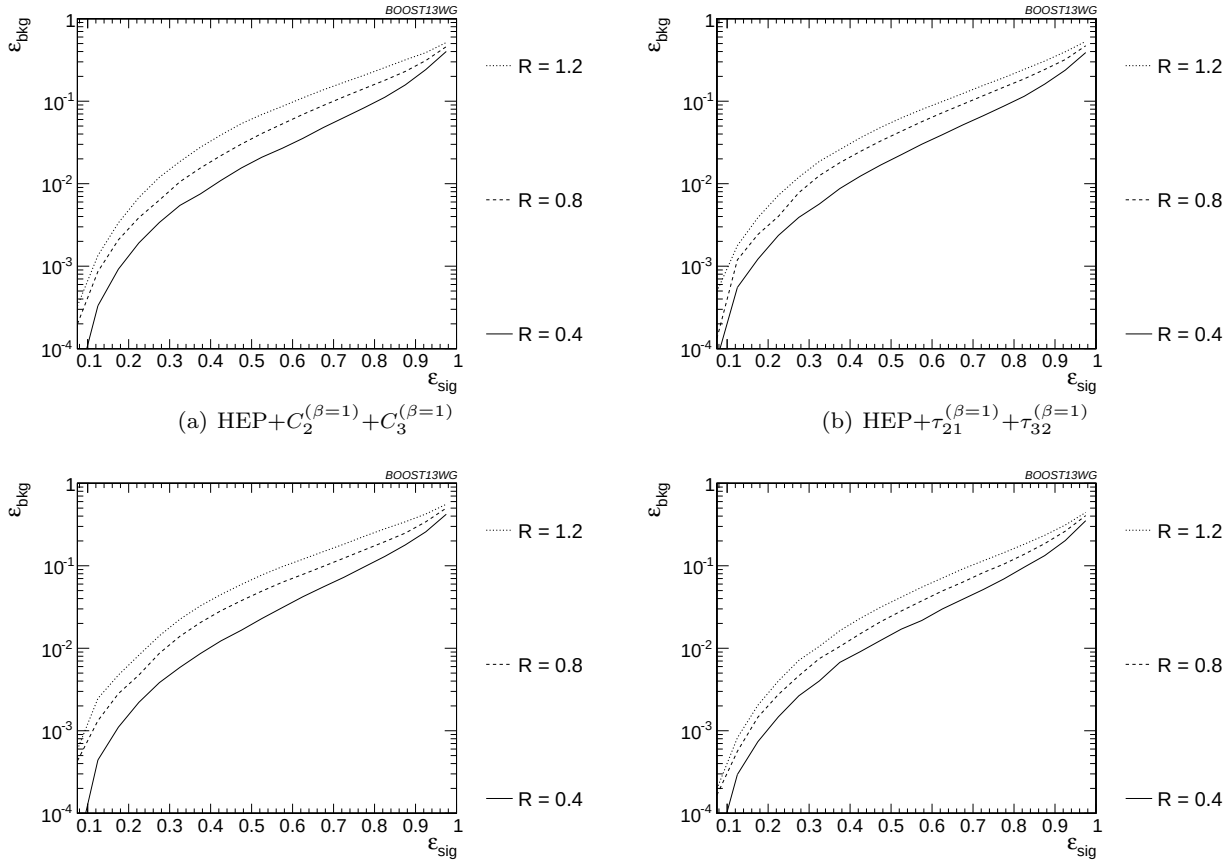

(a) HEP+$C_2^{(\beta=1)}$+$C_3^{(\beta=1)}$

(b) HEP+$\tau_{21}^{(\beta=1)}$+$\tau_{32}^{(\beta=1)}$

(c) HEP + Qjet mass volatility

(d) HEP + all

Fig. 32 Comparison of BDT combination of HEP tagger + shape at different radius at p_T = 1.5-1.6 TeV.

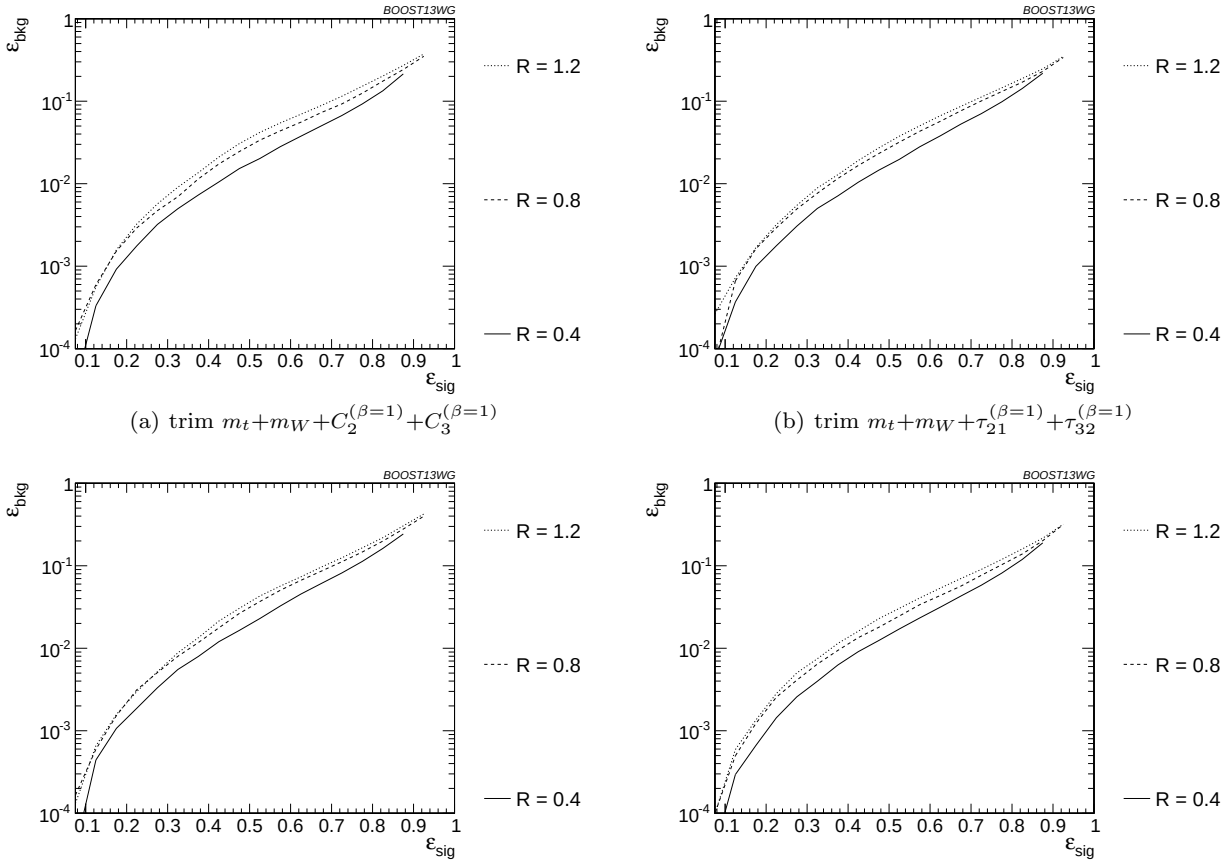

(a) trim m_t+m_W+$C_2^{(\beta=1)}$+$C_3^{(\beta=1)}$

(b) trim m_t+m_W+$\tau_{21}^{(\beta=1)}$+$\tau_{32}^{(\beta=1)}$

(c) trim m_t+m_W + Qjet mass volatility

(d) trim m_t+m_W + all

Fig. 33 Comparison of BDT combination of trimming + shape at different radius at p_T = 1.5-1.6 TeV.

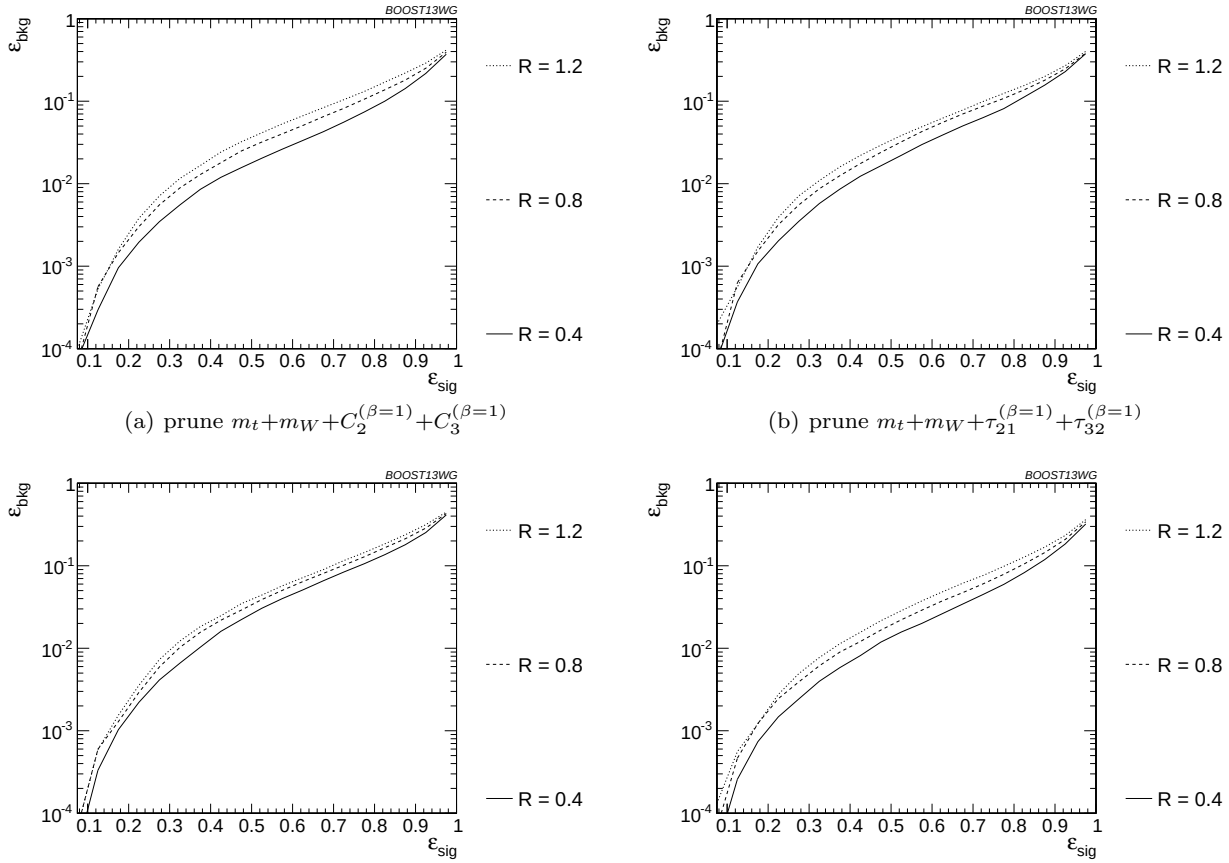

(a) prune m_t+m_W+$C_2^{(\beta=1)}$+$C_3^{(\beta=1)}$

(b) prune m_t+m_W+$\tau_{21}^{(\beta=1)}$+$\tau_{32}^{(\beta=1)}$

(c) prune m_t+m_W + Qjet mass volatility

(d) prune m_t+m_W + all

Fig. 34 Comparison of BDT combination of pruning + shape at different radius at p_T = 1.5-1.6 TeV.

7.4 Performance at Sub-Optimal Working Points

7.4.1 p_T dependence (single variable)

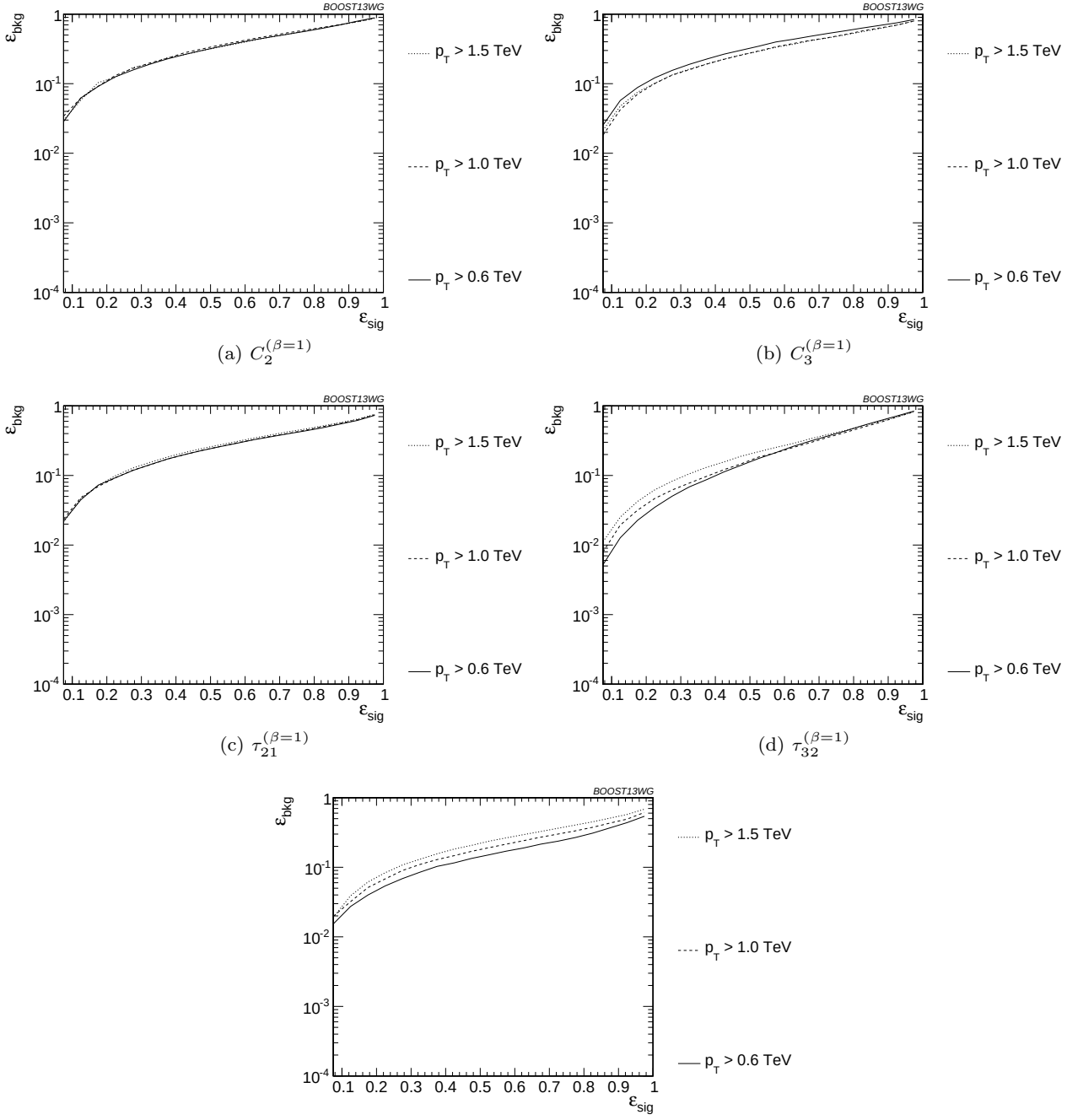

(a) $C_2^{(\beta=1)}$ (b) $C_3^{(\beta=1)}$

(c) $\tau_{21}^{(\beta=1)}$ (d) $\tau_{32}^{(\beta=1)}$

(e) Qjet mass volatility

Fig. 35 Comparison of individual jet shape performance at different p_T using the anti-k_{T} R=0.8 algorithm; the tagger inputs are set to the optimum value for $p_T = 1.5 - 1.6$ TeV.

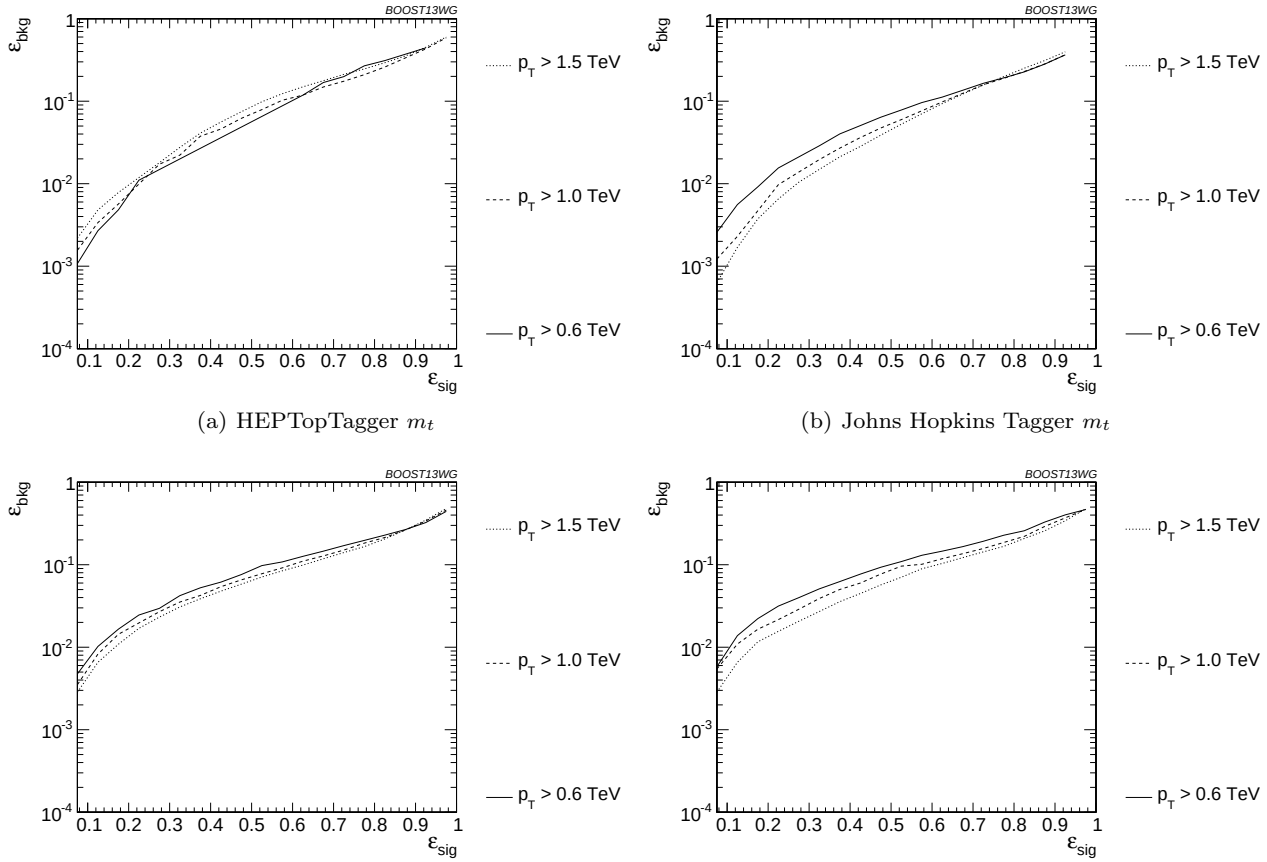

(a) HEPTopTagger m_t

(b) Johns Hopkins Tagger m_t

(c) Pruning m_t

(d) Trimming m_t

Fig. 36 Comparison of top mass performance of different taggers at different p_T using the anti-k_{T} R=0.8 algorithm; the tagger inputs are set to the optimum value for $p_T = 1.5 - 1.6$ TeV.

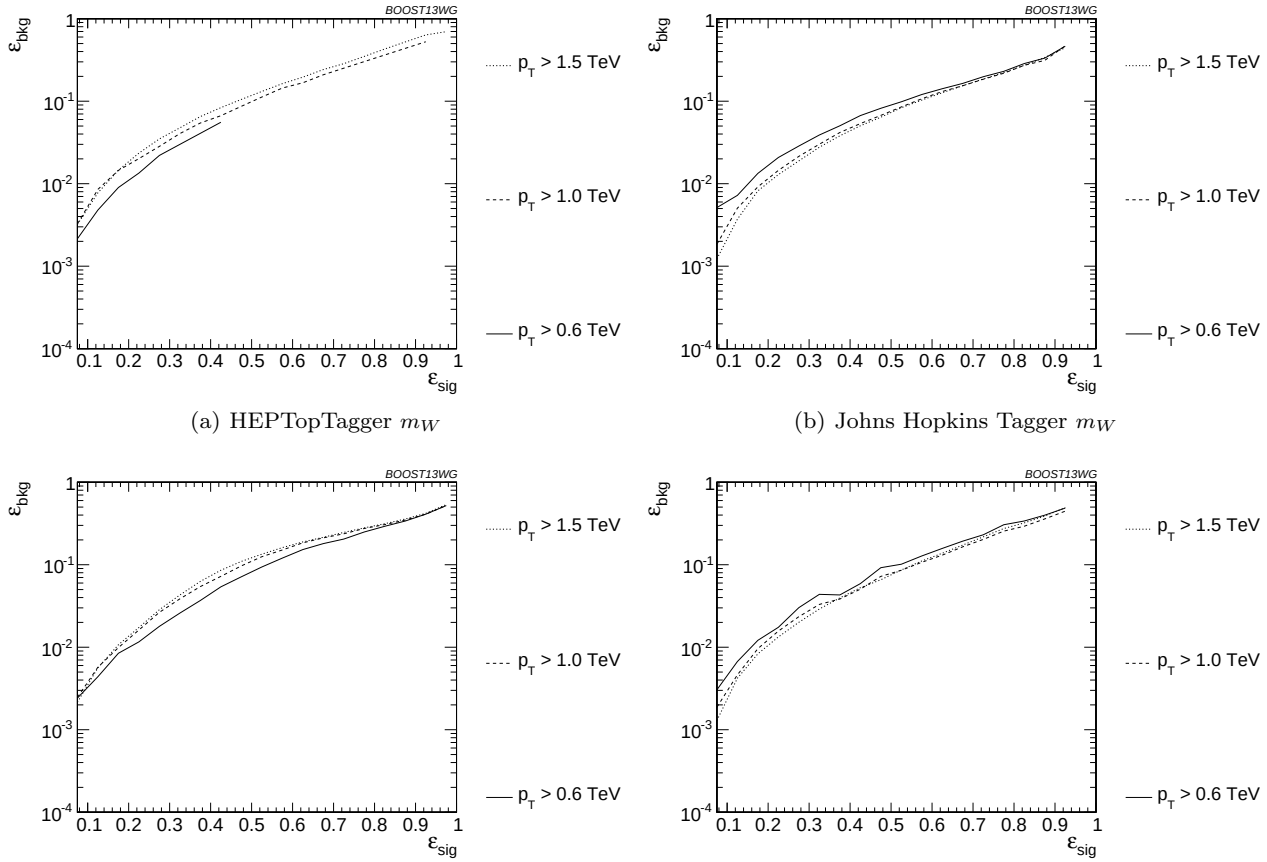

(a) HEPTopTagger m_W

(b) Johns Hopkins Tagger m_W

(c) Pruning m_W

(d) Trimming m_W

Fig. 37 Comparison of W mass performance of different taggers at different p_T using the anti-k_{T} R=0.8 algorithm; the tagger inputs are set to the optimum value for $p_T = 1.5 - 1.6$ TeV.

7.4.2 R dependence (single variable)

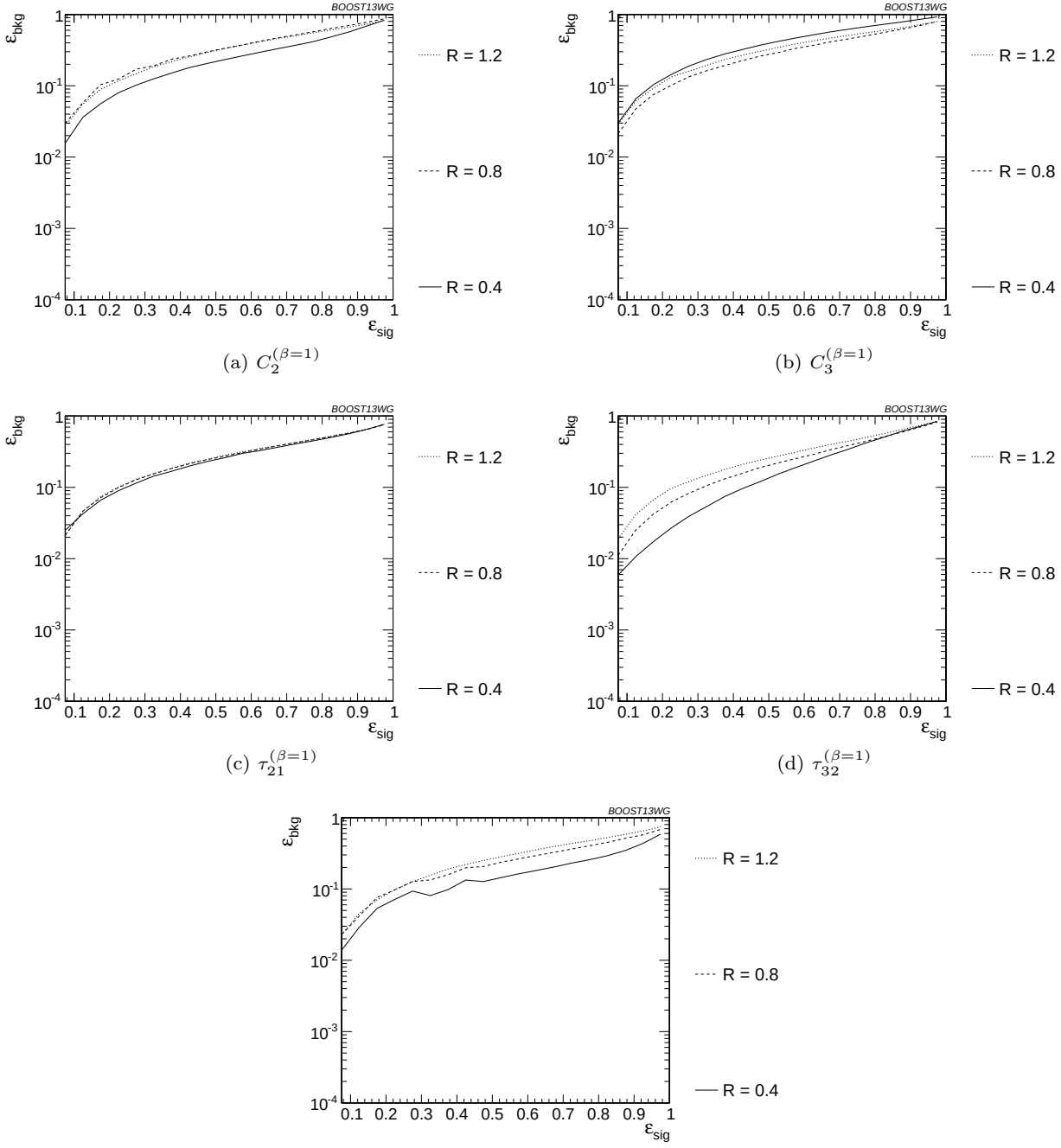

(a) $C_2^{(\beta=1)}$

(b) $C_3^{(\beta=1)}$

(c) $\tau_{21}^{(\beta=1)}$

(d) $\tau_{32}^{(\beta=1)}$

(e) Qjet mass volatility

Fig. 38 Comparison of individual jet shape performance at different R in the $p_T = 1500 - 1600$ GeV bin; the tagger inputs are set to the optimum value for $R = 1.2$ TeV.

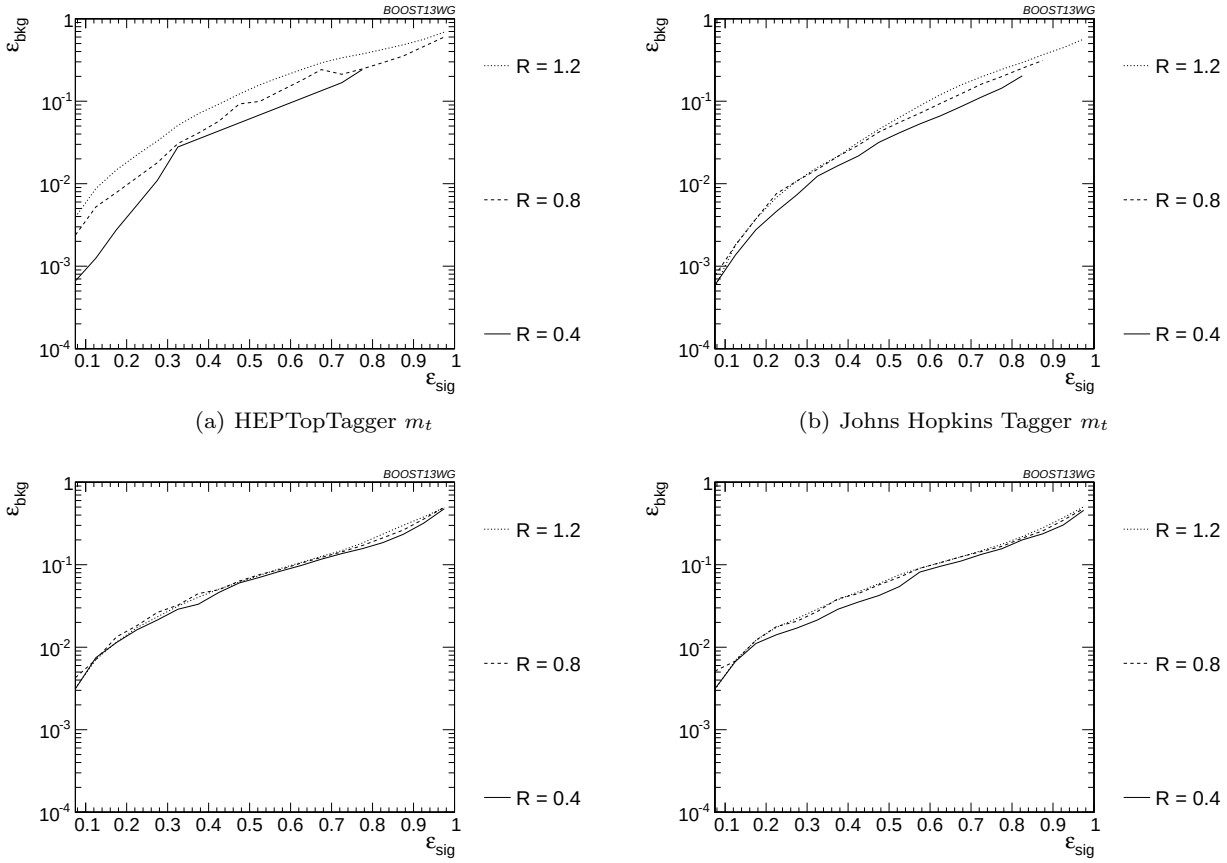

(a) HEPTopTagger m_t

(b) Johns Hopkins Tagger m_t

(c) Pruning m_t

(d) Trimming m_t

Fig. 39 Comparison of top mass performance of different taggers at different R in the $p_T = 1500 - 1600$ GeV bin; the tagger inputs are set to the optimum value for $R = 1.2$ TeV.

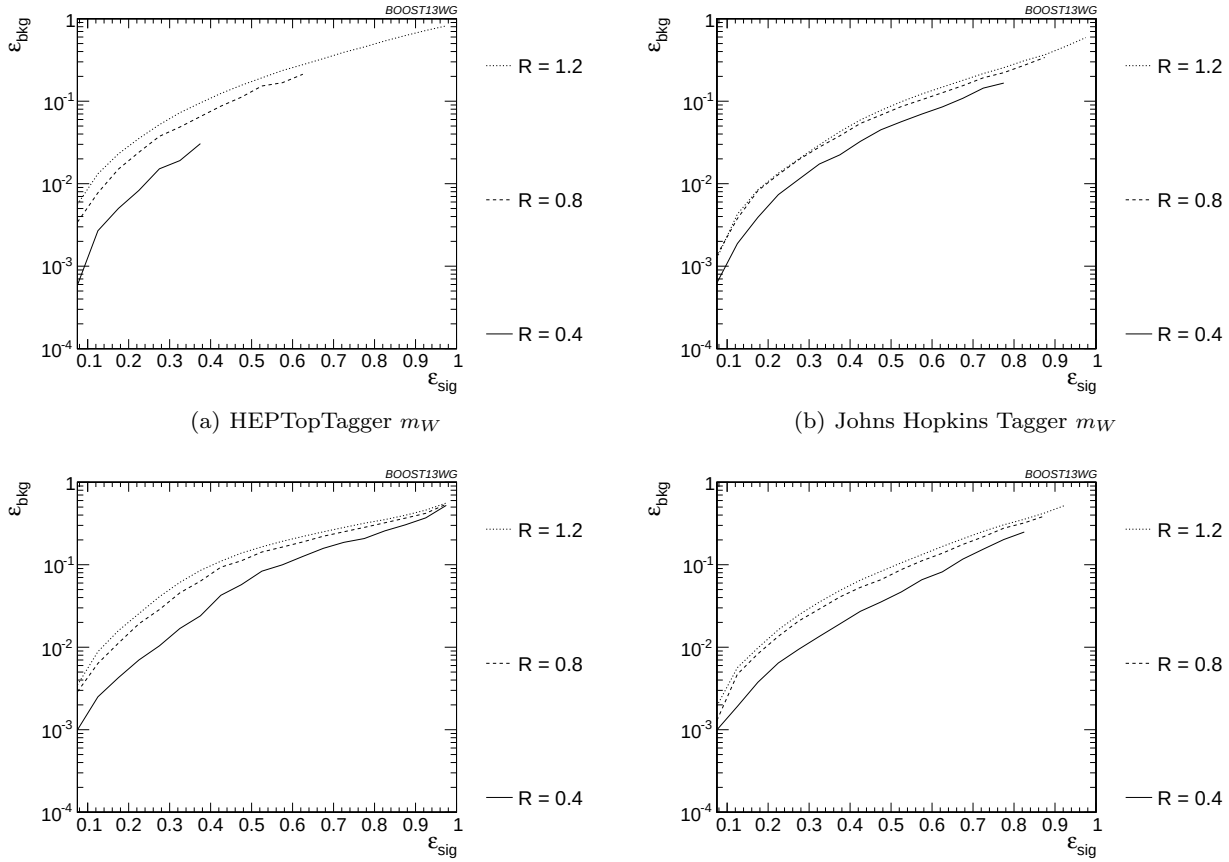

(a) HEPTopTagger m_W

(b) Johns Hopkins Tagger m_W

(c) Pruning m_W

(d) Trimming m_W

Fig. 40 Comparison of W mass performance of different taggers at different R in the $p_T = 1500 - 1600$ GeV bin; the tagger inputs are set to the optimum value for $R = 1.2$ TeV.

7.4.3 p_T dependence

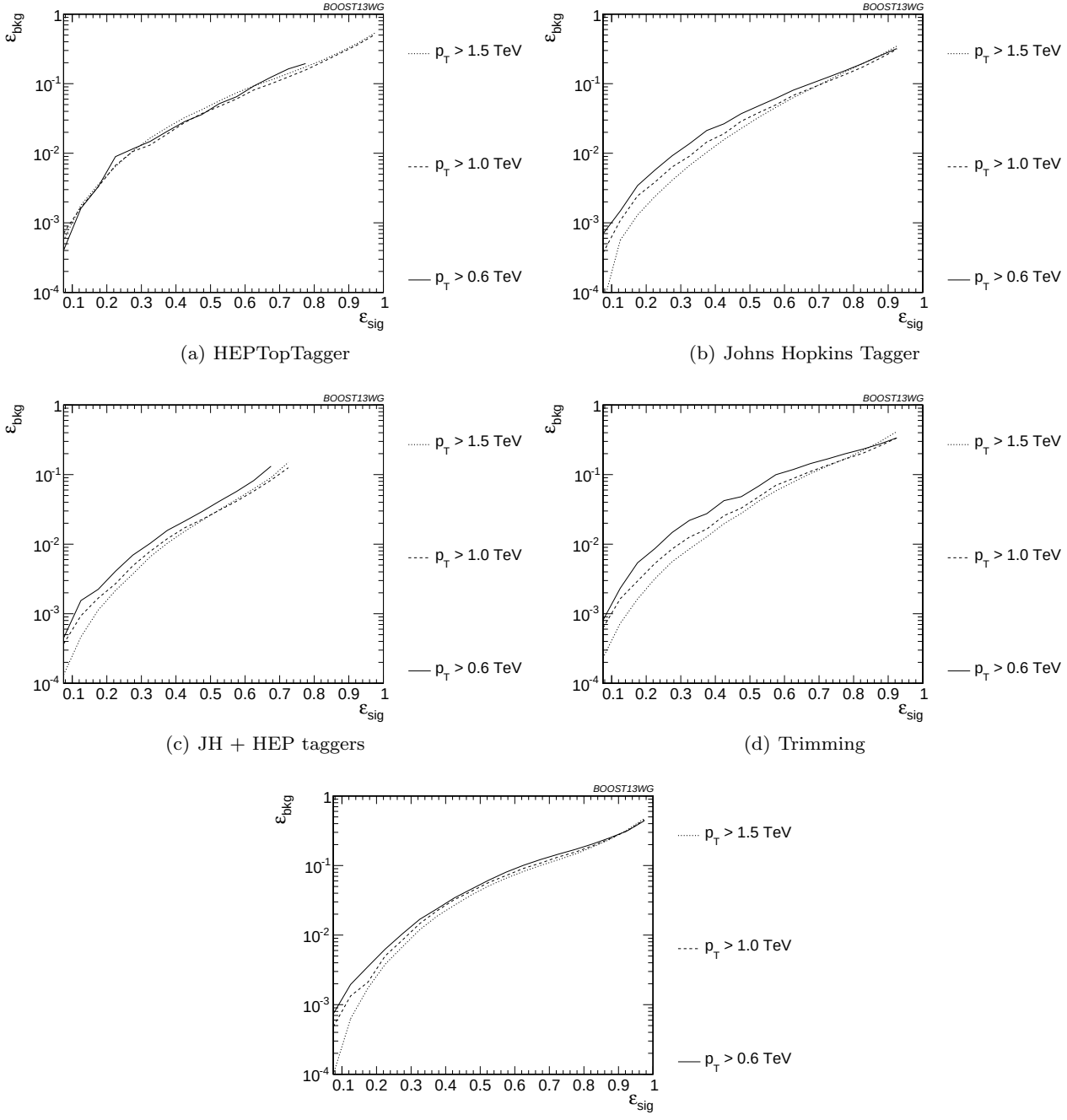

(a) HEPTopTagger

(b) Johns Hopkins Tagger

(c) JH + HEP taggers

(d) Trimming

(e) Pruning

Fig. 41 Comparison of BDT combination of tagger performance at different p_T using the anti-k_T R=0.8 algorithm; the tagger inputs are set to the optimum value for $p_T = 1.5 - 1.6$ TeV.

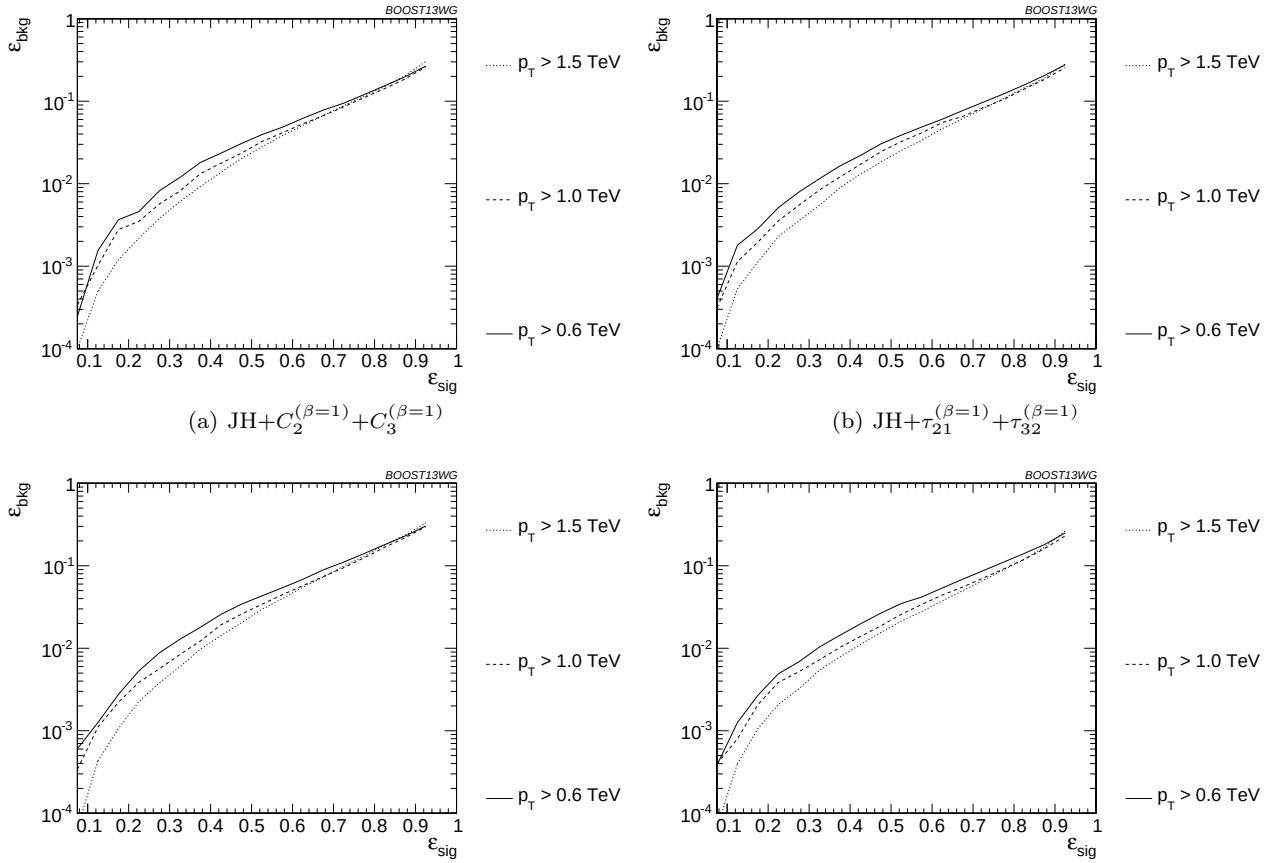

(a) JH+$C_2^{(\beta=1)}$+$C_3^{(\beta=1)}$

(b) JH+$\tau_{21}^{(\beta=1)}$+$\tau_{32}^{(\beta=1)}$

(c) JH + Qjet mass volatility

(d) JH + all

Fig. 42 Comparison of BDT combination of JH tagger + shape at different p_T using the anti-k_{T} R=0.8 algorithm; the tagger inputs are set to the optimum value for $p_T = 1.5 - 1.6$ TeV.

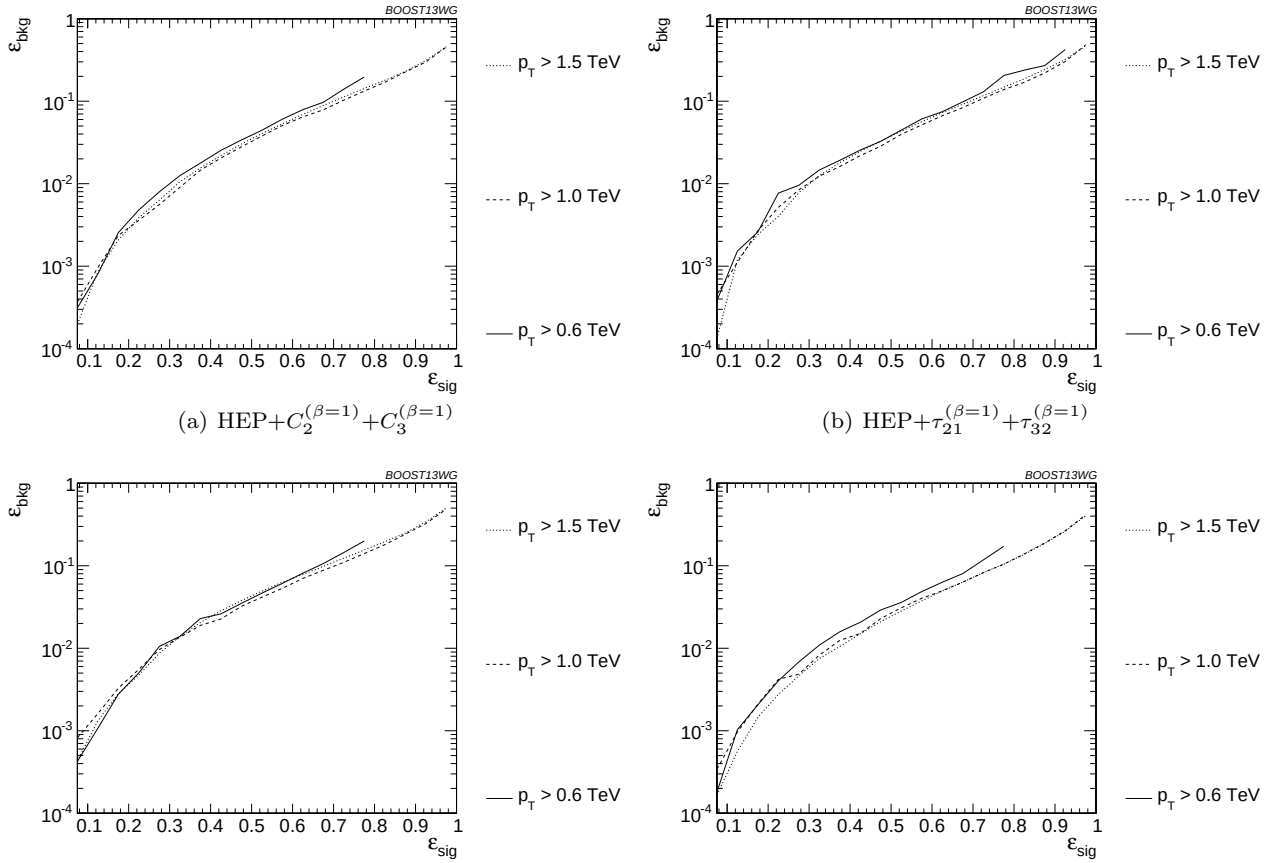

(a) HEP+$C_2^{(\beta=1)}$+$C_3^{(\beta=1)}$

(b) HEP+$\tau_{21}^{(\beta=1)}$+$\tau_{32}^{(\beta=1)}$

(c) HEP + Qjet mass volatility

(d) HEP + all

Fig. 43 Comparison of BDT combination of HEP tagger + shape at different p_T using the anti-k_{T} R=0.8 algorithm; the tagger inputs are set to the optimum value for $p_T = 1.5 - 1.6$ TeV.

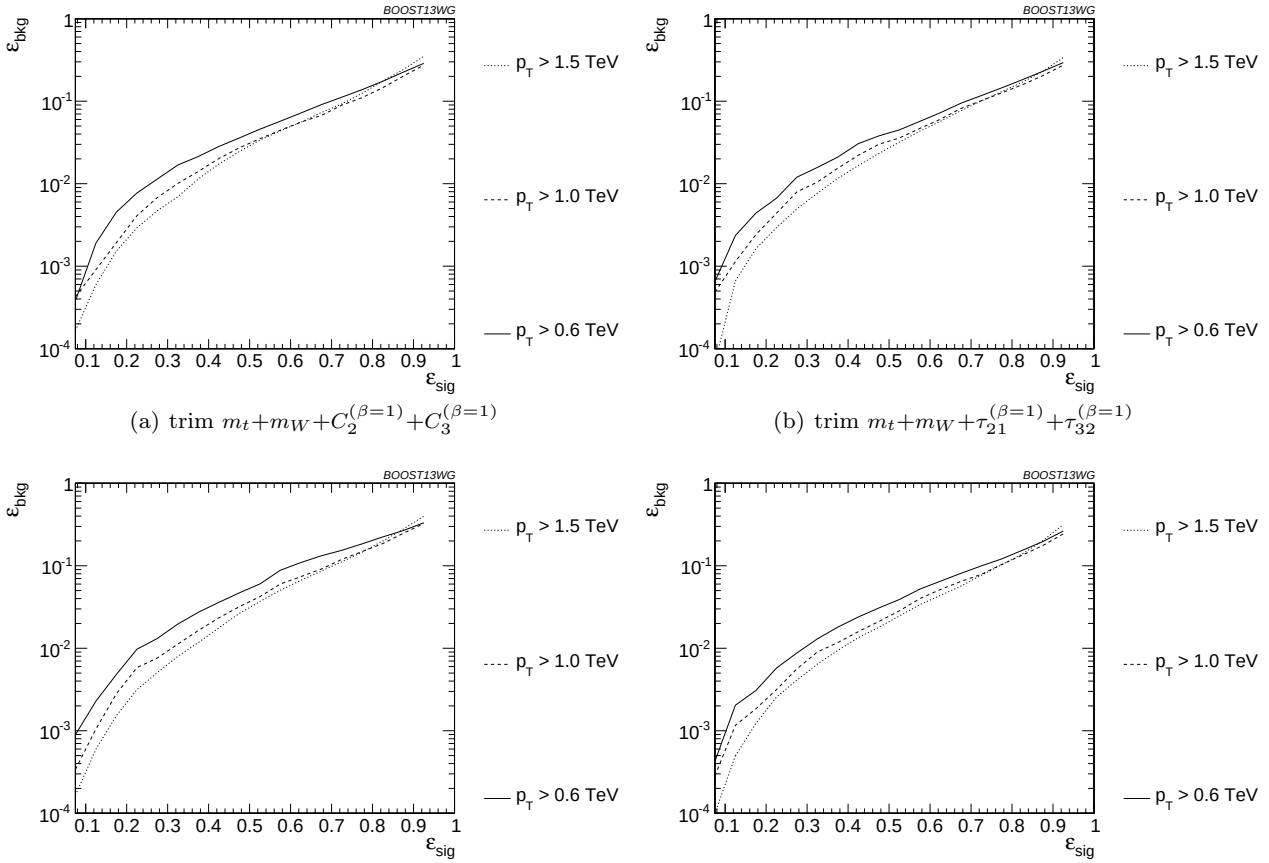

(a) trim m_t+m_W+$C_2^{(\beta=1)}$+$C_3^{(\beta=1)}$

(b) trim m_t+m_W+$\tau_{21}^{(\beta=1)}$+$\tau_{32}^{(\beta=1)}$

(c) trim m_t+m_W + Qjet mass volatility

(d) trim m_t+m_W + all

Fig. 44 Comparison of BDT combination of trimming + shape at different p_T using the anti-k_{T} R=0.8 algorithm; the tagger inputs are set to the optimum value for $p_T = 1.5 - 1.6$ TeV.

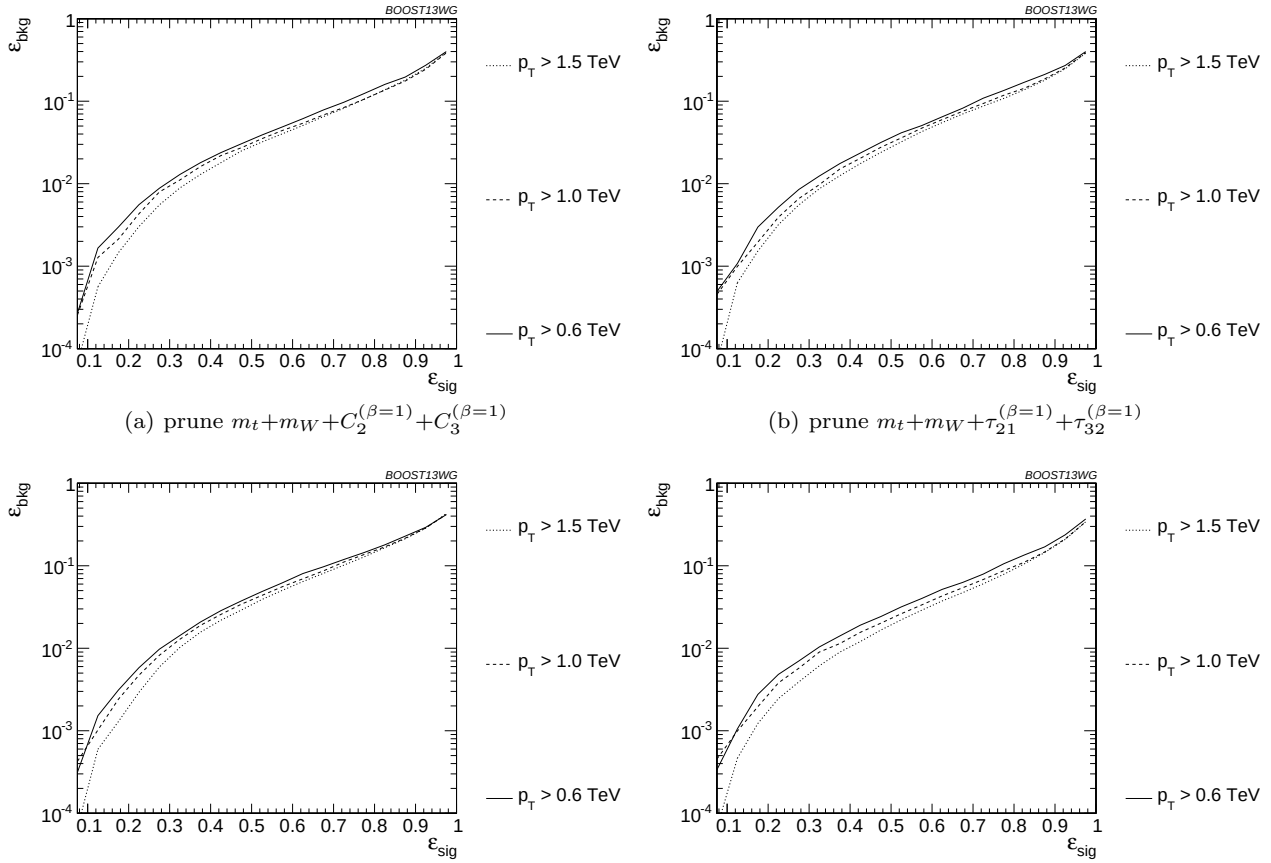

(a) prune m_t+m_W+$C_2^{(\beta=1)}$+$C_3^{(\beta=1)}$

(b) prune m_t+m_W+$\tau_{21}^{(\beta=1)}$+$\tau_{32}^{(\beta=1)}$

(c) prune m_t+m_W + Qjet mass volatility

(d) prune m_t+m_W + all

Fig. 45 Comparison of BDT combination of pruning + shape at different p_T using the anti-k_{T} R=0.8 algorithm; the tagger inputs are set to the optimum value for $p_T = 1.5 - 1.6$ TeV.

7.4.4 R dependence

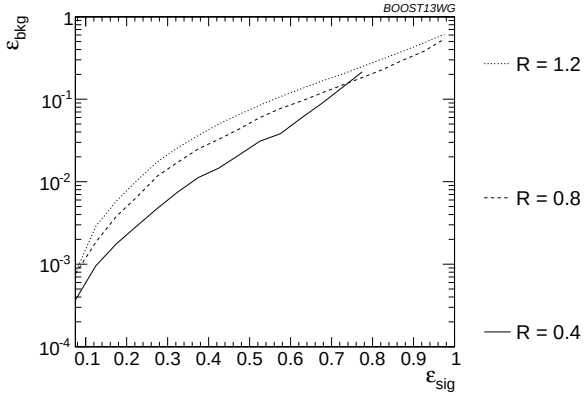

(a) HEPTopTagger

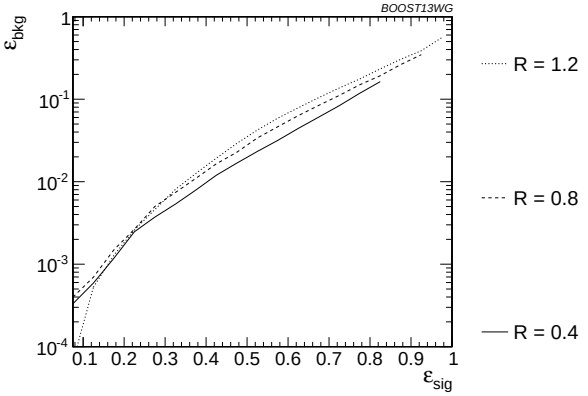

(b) Johns Hopkins Tagger

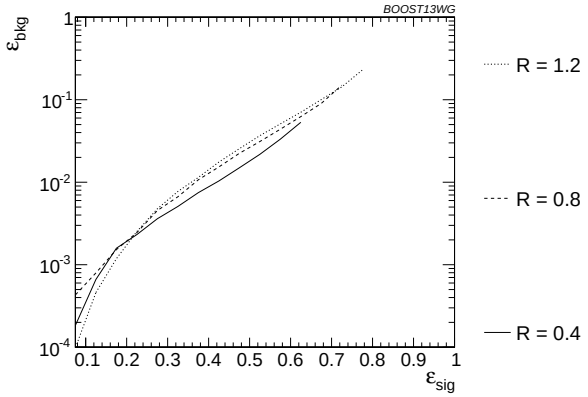

(c) JH + HEP taggers

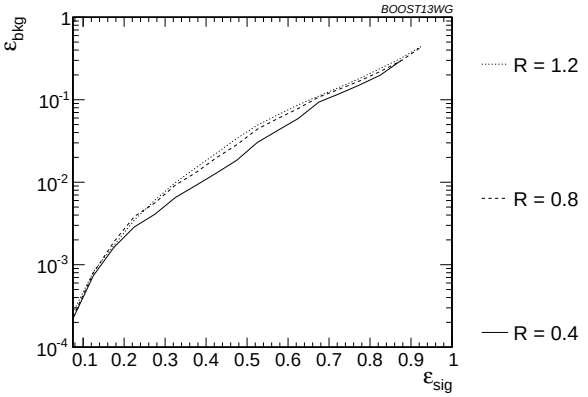

(d) Trimming

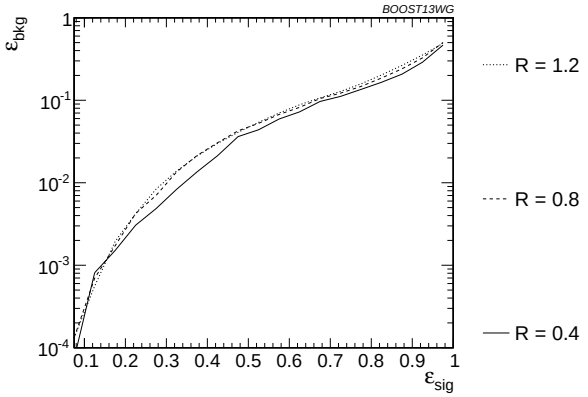

(e) Pruning

Fig. 46 Comparison of tagger and jet shape performance at different radius at p_T = 1.5-1.6 TeV; the tagger inputs are set to the optimum value for $R = 1.2$ TeV.

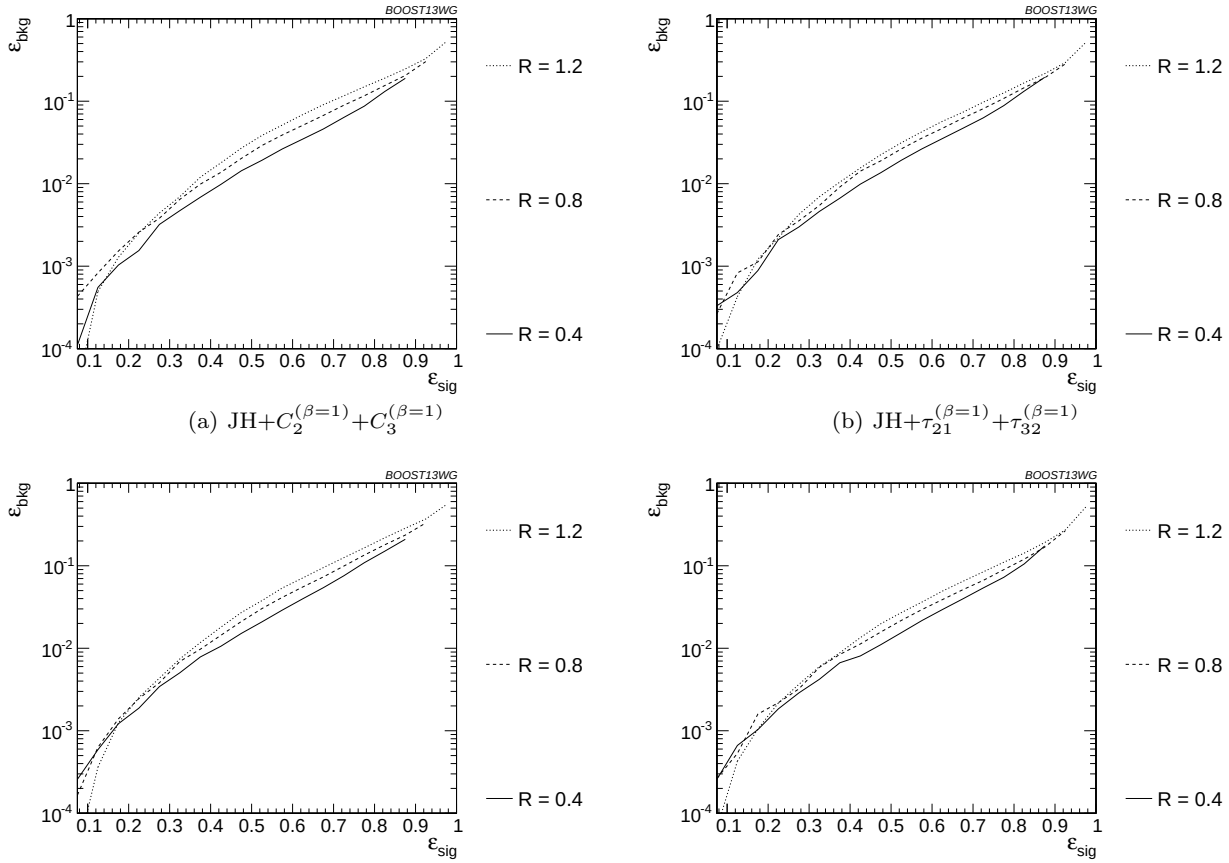

(a) JH+$C_2^{(\beta=1)}$+$C_3^{(\beta=1)}$

(b) JH+$\tau_{21}^{(\beta=1)}$+$\tau_{32}^{(\beta=1)}$

(c) JH + Qjet mass volatility

(d) JH + all

Fig. 47 Comparison of BDT combination of JH tagger + shape at different radius at p_T = 1.5-1.6 TeV; the tagger inputs are set to the optimum value for $R = 1.2$ TeV.

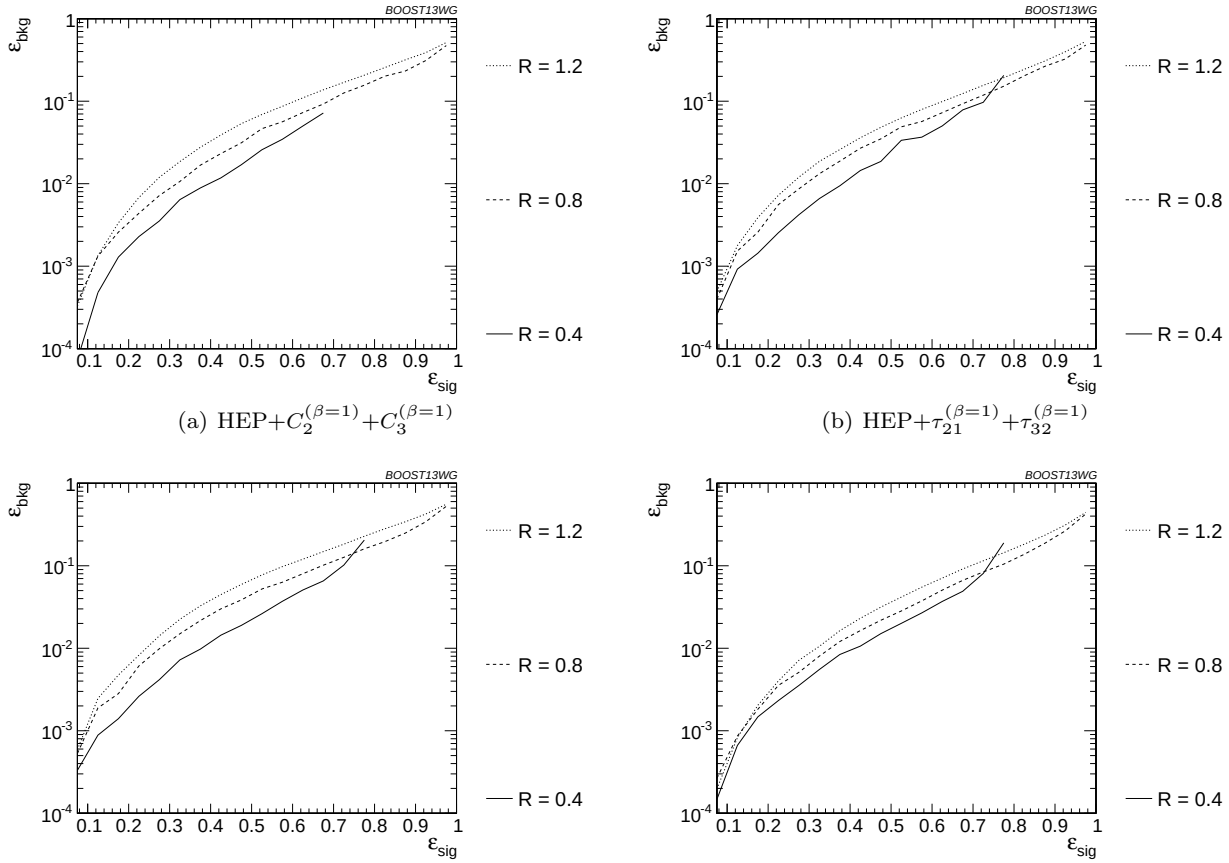

(a) HEP+$C_2^{(\beta=1)}$+$C_3^{(\beta=1)}$

(b) HEP+$\tau_{21}^{(\beta=1)}$+$\tau_{32}^{(\beta=1)}$

(c) HEP + Qjet mass volatility

(d) HEP + all

Fig. 48 Comparison of BDT combination of HEP tagger + shape at different radius at p_T = 1.5-1.6 TeV; the tagger inputs are set to the optimum value for $R = 1.2$ TeV.

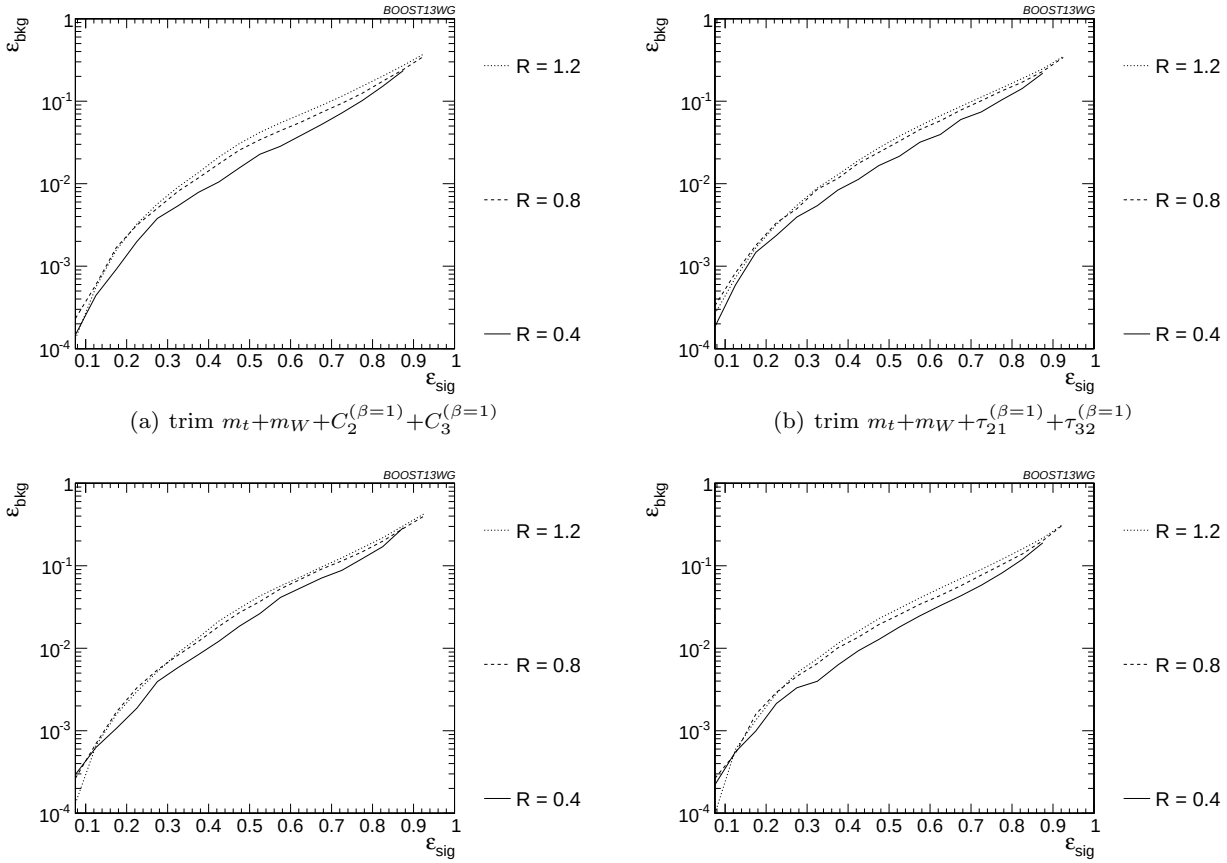

(a) trim m_t+m_W+$C_2^{(\beta=1)}$+$C_3^{(\beta=1)}$

(b) trim m_t+m_W+$\tau_{21}^{(\beta=1)}$+$\tau_{32}^{(\beta=1)}$

(c) trim m_t+m_W + Qjet mass volatility

(d) trim m_t+m_W + all

Fig. 49 Comparison of BDT combination of trimming + shape at different radius at p_T = 1.5-1.6 TeV; the tagger inputs are set to the optimum value for $R = 1.2$ TeV.

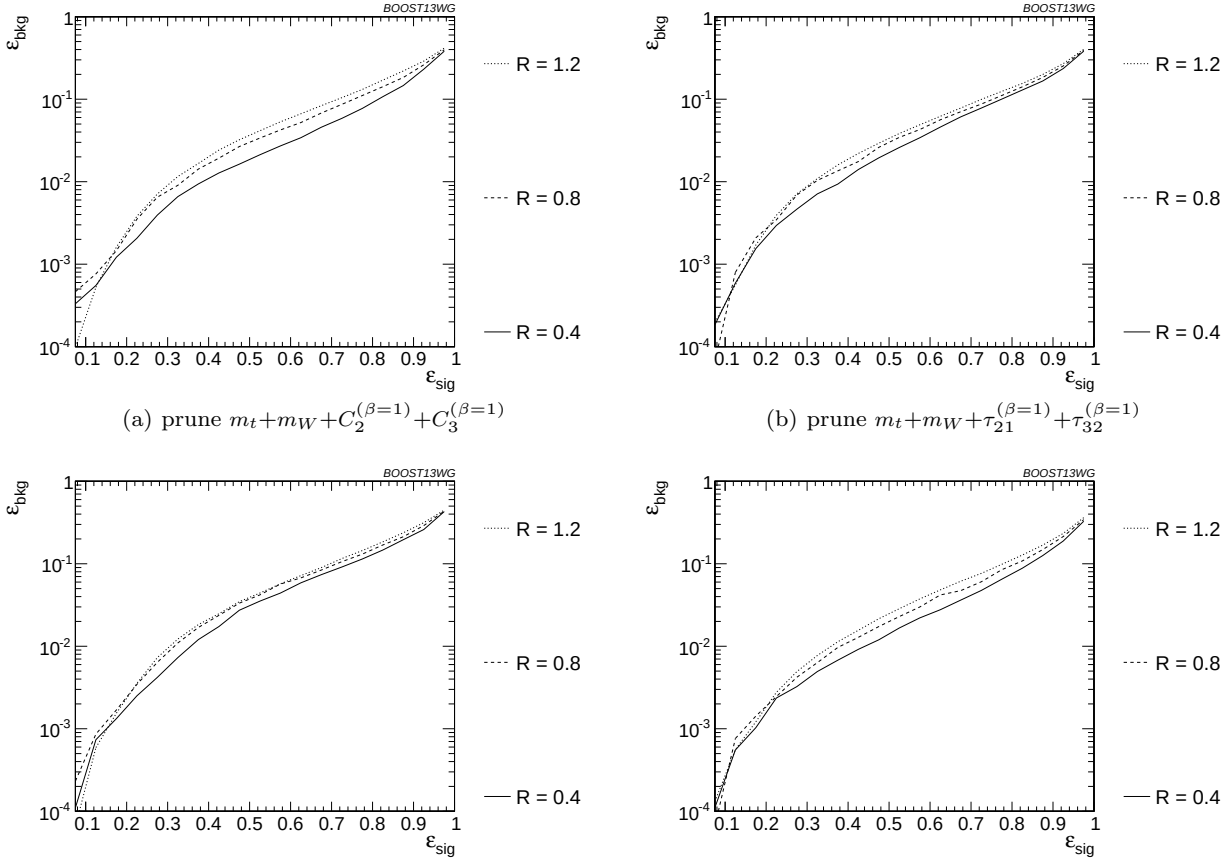

(a) prune m_t+m_W+$C_2^{(\beta=1)}$+$C_3^{(\beta=1)}$

(b) prune m_t+m_W+$\tau_{21}^{(\beta=1)}$+$\tau_{32}^{(\beta=1)}$

(c) prune m_t+m_W + Qjet mass volatility

(d) prune m_t+m_W + all

Fig. 50 Comparison of BDT combination of pruning + shape at different radius at p_T = 1.5-1.6 TeV; the tagger inputs are set to the optimum value for $R = 1.2$ TeV.

8 Summary & Conclusions

This report discussed the correlations between observables and looked forward to jet substructure at Run II of the LHC at 14 TeV center-of-mass collisions eneergies.

Acknowledgements

We thank the Department of Physics at the University of Arizona and for hosting the conference at the Little America Hotel. We also thank Harvard University for hosting the event samples used in this report. We also thank Hallie Bolonkin for the BOOST2013 poster design and Jackson Boelts' ART465 class (fall 2012) at the University of Arizona School of Arts VisCom program. (NEED TO ASK PETER LOCH FOR MORE ACKNOWLEDGEMENTS)

References

1. A. Abdesselam, E. B. Kuutmann, U. Bitenc, G. Brooijmans, J. Butterworth, et al., *Boosted objects: A Probe of beyond the Standard Model physics*, *Eur.Phys.J.* **C71** (2011) 1661, [arXiv:1012.5412].
2. A. Altheimer, S. Arora, L. Asquith, G. Brooijmans, J. Butterworth, et al., *Jet Substructure at the Tevatron and LHC: New results, new tools, new benchmarks*, *J.Phys.* **G39** (2012) 063001, [arXiv:1201.0008].
3. A. Altheimer, A. Arce, L. Asquith, J. Backus Mayes, E. Bergeaas Kuutmann, et al., *Boosted objects and jet substructure at the LHC*, arXiv:1311.2708.
4. C. Anders, C. Bernaciak, G. Kasieczka, T. Plehn, and T. Schell, *Benchmarking an Even Better HEPTopTagger*, *Phys.Rev.* **D89** (2014) 074047, [arXiv:1312.1504].